Frontal Subduction of the Mid-Atlantic Bight Shelf Water at the Onshore Edge of a Warm-Core Ring

Authors: **Weifeng (Gordon) Zhang[1] and Jacob Partida[2]**

[1]Applied Ocean Physics and Engineering Department, Woods Hole Oceanographic Institution,
266 Woods Hole Road, Woods Hole, MA, USA

[2]Humboldt State University, Arcata, California, USA

Corresponding author: Weifeng (Gordon) Zhang (wzhang@whoi.edu)

Key Points:

1. Observations show subduction of shelf water at the onshore edge of a warm-core ring that impinges on the Mid-Atlantic Bight shelf break
2. The submesoscale frontal subduction of the shelf water at the shelf break results from the frontogenesis process on the ring edge
3. The subducted shelf water is transported offshore underneath a surface layer of ring water by the strong ring-edge current

Abstract

This work studies the subduction of the shelf water along the onshore edge of a warm-core ring (WCR) that impinges on the edge of the Mid-Atlantic Bight continental shelf. The dynamical analysis is based on observations by satellites and from the Ocean Observatories Initiative Pioneer Array observatory as well as idealized numerical model simulations. They together show that frontogenesis-induced submesoscale frontal subduction with order-one Rossby and Froude numbers occurs on the onshore edge of the ring. The subduction flow results from the onshore migration of the WCR that intensifies the density front on the interface of the ring and shelf waters. The subduction is a part of the cross-front secondary circulation trying to relax the intensifying density front. The dramatically different physical and biogeochemical properties of the ring and shelf waters provide a great opportunity to visualize the subduction phenomenon. Entrained by the ring-edge current, the subducted shelf water is subsequently transported offshore below a surface layer of ring water and alongside of the surface-visible shelf-water streamer. It explains the historical observations of isolated subsurface packets of shelf water along the ring periphery in the slope sea. Model-based estimate suggests that this type of subduction-associated subsurface cross-shelfbreak transport of the shelf water could be substantial relative to other major forms of shelfbreak water exchange. This study also proposes that outward spreading of the ring-edge front by the frontal subduction may facilitate entrainment of the shelf water by the ring-edge current and enhances the shelf-water streamer transport at the shelf edge.

1. Introduction

1.1 Mid-Atlantic Bight Shelfbreak Circulation

The Mid-Atlantic Bight (MAB) shelf break off the US northeast coast sits between the relatively cold, fresh shelf water and the warm, saline offshore waters (e.g., Chapman and Beardsley 1989; Houghton et al. 2009; Linder and Gawarkiewicz 1998). A prominent *retrograde* shelfbreak density front (isopycnals shoaling toward offshore) marks the boundary between the shelf and slope waters, with clear temperature and salinity signatures (e.g., Houghton et al. 1988; Zhang et al. 2011). The shelf water is generally less dense than the slope water, as the shelfbreak salinity difference often dominates the density variation. However, the cross-shelfbreak density gradient can be reversed, especially at times of Gulf Stream warm-core rings (WCR) impinging on the shelf edge (e.g., Zhang and Gawarkiewicz 2015a) forming a *prograde* density front (isopycnals shoaling toward inshore). The dramatic temperature difference between the shelf and ring waters can outweigh the salinity effect and make the shelf water denser than the adjacent ring water.

In this study, the waters in the shelfbreak region are divided into three general categories: i) shelf water, defined as *potential* temperature <14°C and *absolute* salinity <34.7 g kg^{-1}, corresponding to the water onshore of the MAB shelfbreak front in springtime (Linder and Gawarkiewicz 1998; Zhang et al. 2011); ii) ring water with near-surface *potential* temperature >19°C and *absolute* salinity >36 g kg^{-1}; and iii) slope water with properties between. Note that salinity presented here is absolute salinity (McDougall et al. 2012).

Despite the topographic constraint and the shelfbreak front, there is onshore and offshore transport of waters across the shelf edge, representing the exchange of the shelf and offshore waters that is important for the heat and salt balances on the continental shelf (Lentz 2008). There are different types of shelfbreak exchange, including surface Ekman transport (Gawarkiewicz et al. 1996), pycnocline onshore intrusion of the slope water (Lentz 2003), frontal eddy transport (Gawarkiewicz et al. 2004), Pinochio's Nose onshore intrusion (PNI) of the WCR water (Zhang and Gawarkiewicz 2015a), and shelf-water offshore streamer transport (e.g., Garfield and Evans 1987; Joyce 1991).

Both the PNI and streamers have distinct surface signatures that are visible to satellites. The former is an elongated feature of WCR water extending equator-ward along the shelf break, and the latter is a cold filament of shelf water wrapping around the WCR in the slope sea. They both can transport a substantial amount of water across the shelf break. The onshore transport of ring water in a 2014 PNI event was ~0.22 Sv (Zhang and Gawarkiewicz 2015a); the cross-shelfbreak offshore transport of the shelf water in a 2006 streamer was ~0.28 Sv (Chen et al. 2014). Studies argued that the shelf-water streamer results from entrainment by the WCR (e.g., Joyce et al. 1992; Schlitz 2003). Using a model with no shelfbreak front and no distinction between the shelf and slope waters, Cherian and Brink (2016, 2018) showed that the entrainment of the water on the shelf by the WCR is a barotropic process driven by onshore motion of the ring water. When applied to the northern MAB (Fig. 1), the barotropic process would create a northeastward sea level setdown in the ring-shelf contact region. The associated barotropic pressure gradient force to the north of the WCR would drive an eastward jet of several tens of kilometer (~40 km for MAB) wide through the geostrophic balance and

88 move shelf water toward the streamer; the eastward barotropic pressure gradient force at
89 the eastern end of the ring-shelf contact region would drive an offshore flow of the shelf
90 water and form the streamer. But how the strong baroclinicity at the MAB shelf break,
91 particularly, the presence of the shelfbreak front, affects this shelf-water entrainment
92 process remains unclear.

93 The WCR-induced cross-shelfbreak offshore transport of the shelf water can also
94 occur below the sea surface. Observations have shown subsurface fluxes of shelf water
95 on the ring periphery alongside of surface-visible shelf-water streamers (e.g., Churchill et
96 al. 1986; Kupferman and Garfield 1977; Tang et al. 1985). The model of Cherian and
97 Brink (2016) produces a type of subsurface offshore flux of the shelf-slope water, and
98 they attribute it to the along-isopycnal sinking of the shelf-slope water. But no
99 mechanism is provided to explain the along-isopycnal sinking, and the dynamics of the
100 WCR-induced subsurface shelf-water offshore transport remains unclear. This study
101 focuses on the subsurface cross-shelfbreak offshore transport of the shelf water that starts
102 with frontogenesis-induced shelf water subduction at the *prograde* density front along the
103 northern edge of an onshore-impinging WCR. Note that the ring edge here refers to the
104 temperature and salinity boundary of the ring where the velocity starts to increase.

105 *1.2 Frontal Subduction and Filament*

106 The dynamics of frontal subduction has been investigated in the atmosphere and
107 open ocean as an ageostrophic, submesoscale phenomenon associated with frontogenesis
108 (e.g., Hoskins 1982; Levy et al. 2001; Mahadevan and Tandon 2006; Spall 1995). An
109 ocean submesoscale phenomenon is characterized by Rossby number,

110 $$Ro = \frac{U}{fL_c}, \quad (1)$$

and Froude number,

$$Fr = \frac{U}{NH}, \tag{2}$$

both being $O(1)$ (McWilliams 2016). Here, U is the frontal velocity scale; f is the Coriolis parameter; N is the buoyancy frequency; L_c and H are the cross-frontal and vertical length scales of the submesoscale frontal subduction, respectively. Furthermore, L_c is generally smaller than the first baroclinic Rossby radius of deformation

$$L_R = \frac{NH_r}{f}, \tag{3}$$

where H_r is the vertical length scale of the mesoscale process (e.g, WCRs). H_r is generally greater than the vertical length scale of submesoscale processes, i.e., $H_r > H$.

The vertical flow associated with ageostrophic frontal subduction can transport surface tracers downward creating slanted three-dimensional (3D) *along-isopycnal* tracer filaments with strong horizontal gradients (Omand et al. 2015). A related but different process is the horizontal stirring of a geostrophic shear flow that, even with no vertical velocity, can strain the tracer field, intensify existing along-isopycnal tracer gradients (e.g., spiciness) at depth, and result in subsurface, slanted, *cross-isopycnal*-appearing tracer filament (Smith and Ferrari 2009). The increase of the tracer horizontal gradient by this geostrophic shear stirring can be described as

$$\frac{D\nabla C}{Dt} = -\boldsymbol{\sigma}\nabla C, \tag{4}$$

where, C is the tracer concentration, $\sigma_{ij} \equiv \partial u_i/\partial x_j$ is the horizontal strain tensor, and $\boldsymbol{\nabla}$= (∂x, ∂y, ∂z). Presumably, geostrophic shear stirring and frontal subduction could occur simultaneously in a frontal region and form subsurface slanted 3D tracer layers.

At the MAB shelf break, bathymetry exerts strong influence on circulation (e.g., Cherian and Brink 2016; Zhang and Gawarkiewicz 2015b). Whether the bathymetry affect the frontal subduction and geostrophic shear stirring is unclear. This study shows that the frontal behaviors at the shelf break are similar to those in the open ocean and that shelf water is subducted at the intensifying density front at the onshore edge of the WCR and then transported offshore. The shelf-water subduction and cross-shelfbreak offshore transport occur beneath a surface layer of ring water and thus cannot be detected by satellites. Subsurface measurements of the Ocean Observatories Initiative (OOI) Pioneer Array observatory at the northern MAB shelf break (Gawarkiewicz and Plueddemann 2018) provides a great opportunity for studies of the frontal subduction process.

2. Methods

2.1 Observations

This study uses data from satellites and the OOI Pioneer Array (see Gawarkiewicz and Plueddemann 2018 for the specifics about its instrumentation). Sea surface temperature (SST) from single-pass snapshots taken by different satellites with a horizontal resolution of 1 km is used here to provide the regional context. The different surface temperature of the ring, slope and shelf waters during the study period of June 2014 make SST an effective tool for distinguishing the water masses.

In situ measurements in June 2014 from the Pioneer Array, including temperature, salinity, dissolved oxygen (DO), and colored dissolved organic matter (CDOM), and velocity data from McLane moored profilers at the Central Inshore (CI), Central Offshore (CO) and Offshore (OS) moorings and from the Eastern Boundary (EB) and Frontal Zone

(FZ) gliders, are downloaded from the NSF OOI data portal[1] and presented here. The CI, CO and OS moorings are located on the western mooring line of 70.883°W at respective water depths of 127, 147 and 450 m (Fig. 1). The McLane profilers on them take a vertical profile every 1.5, 1.5 and 3 hours, respectively, and the downloaded data have a vertical resolution of 1.5 m. The cross-shelf EB glider line is located 80 km to the east of the moorings (Fig. 1b); the FZ glider line is oriented in the along-shelf direction (Fig. 1d). The gliders sample the water column with the horizontal interval of 200 – 2000 m, depending on the local water depth, and report data in the vertical resolution of 0.3 m.

The ADCP horizontal velocity data from the CO mooring is presented here to show the ring-edge flow The ADCP has the vertical bin size of 4 m and the time-average window of 15 minutes. A low-pass filter with a 5-day Lanczos window (with half-power point at $\pm$1.5 days) is applied to the ADCP data at each depth to remove the strong internal wave signals that are ubiquitous in the Pioneer Array velocity data and hinder the data interpretation. This filter not only removes the internal wave signals but also smooths the signals associated with the fast-moving ring edge. However, because the ring signal lasts for at least several days, the lower-frequency signature of the WCR remains visible (see below). We here present both raw and filtered horizontal velocity data with u and v representing eastward and northward components of the velocity, respectively.

2.2 Modeling

The Regional Ocean Modeling System (Shchepetkin and McWilliams 2008) with an idealized configuration is used in this study. The model solves nonlinear Boussinesq hydrostatic momentum equations and a single density equation. The model configuration

[1] http://ooinet.oceanobservatories.org

177 is similar to that in Zhang and Gawarkiewicz (2015a, 2015b). It has an idealized
178 rectangular domain with the area of 2010.5 km (in x and along-shelf) × 479 km (in y and
179 cross-shelf). The origin of the coordinate is at the center point of the northern coastal
180 boundary. The model horizontal resolution is 500 m in both x and y directions in the
181 central study region of 500 km×350 km and decreases to 2 km on the outer boundaries.
182 There are 60 terrain-following vertical layers with thinner layers towards the surface and
183 bottom. The model bathymetry is uniform in the along-shelf (x) direction. Its cross-shelf
184 variation in y direction is an idealized MAB shelfbreak bathymetry (Fig. 2b):

191 $$h = max\left(0, h_f \frac{y_p + l_f - y}{y_p + l_f}\right) + h_{p1} tanh \frac{y - y_p}{l_p} - h_{p2}. \quad (5)$$

185 Here, the shelf width scale l_f = 41 km, y-coordinate of the center of the slope y_p = –170.5
186 km, the cross-shelf length scale of the slope l_p = 16.5 km, the shelf depth scale h_f = 65 m,
187 the slope vertical scales h_{p1} = 465 m and h_{p2} = 540 m. The bathymetry starts from 10-m
188 deep on the northern coast, deepens southward with a slope of $\alpha \approx 0.5\times10^{-3}$ to the 100-m
189 isobath at $y \approx$ –140 km, and then transitions to a hyperbolic-tangent-shaped continental
190 slope with a maximum depth of 1005 m.

192 Along-shelf periodic boundary conditions are applied in all simulations.
193 Horizontal explicit viscosity and diffusivity are 0 in the 500 km×350 km study area and
194 increase outward reaching 100 m^2s^{-1} on the western, southern and eastern boundaries. A
195 general length scale vertical turbulence closure *k-kl* scheme (Warner et al. 2005) and
196 quadratic bottom drag with coefficient of 0.003 are used. There is no surface forcing.

197 The model initial density consists of an idealized retrograde shelfbreak front
198 separating the shelf and slope waters and an idealized circular WCR residing in the slope
199 water (Fig. 2). The density of the slope water is horizontally uniform and varies

vertically. Its vertical profile is based on an observed profile in the MAB slope sea with surface density of ρ_{sl} = 1026.7 kg m^{-3}. The shelf water with surface density of ρ_{sh} is characterized by negative, along-shelf uniform density anomaly relative to the slope water. The cross-shelf density gradient forms a shelfbreak front with isopycnals rising from the ocean floor toward offshore (Zhang and Gawarkiewicz 2015b).

The WCR has a density anomaly relative to the slope water (Fig. 2a) specified by

$$\Delta\rho_r(x,y,z) = \frac{1}{2}\left[1 - \tanh\left(\frac{r - r_c}{r_b}\right)\right] e^{-\frac{z^2}{H_r^2}} \Delta\rho_0. \quad (6)$$

Here, $\Delta\rho_0$ is the surface density anomaly at the ring center, (x_0, y_0); $r = [(x\text{-}x_0)^2+(y\text{-}y_0)^2]^{1/2}$; r_c is the ring radius to the maximum velocity; r_b is the horizontal length scale of the ring-edge transition region; H_r is the ring vertical scale.

In the control simulation $f = f_0 = 9.37\times10^{-5}$ s^{-1} (40°N; f-plane); ρ_{sh} = 1026.2 kg m^{-3}; x_0 = 0 km and y_0 = −245 km; r_c = 75 km, r_b = 15 km; H_r = 500 m; $\Delta\rho_0$ = −1 kg m^{-3}, resembling the observed density difference between the ring and slope waters. These parameters together give a Burger number of the ring, $NH_r/(fr_c)$, of about 0.7. Here, $N \approx$ 0.01 s^{-1}. The surface density of the ring water $\rho_r = \rho_{sl} + \Delta\rho_0$ = 1025.7 kg m^{-3}. On the sea surface $\rho_r < \rho_{sh} < \rho_{sl}$, consistent with the observed density contrasts among the ring, shelf and slope waters (Zhang and Gawarkiewicz 2015a). The density distribution across the shelfbreak front resembles a typical MAB shelfbreak frontal structure in winter and spring (e.g., Fratantoni et al. 2001; Gawarkiewicz et al. 2001).

Thermal-wind balanced horizontal velocity (assuming zero bottom velocity) and geostrophically balanced sea level tilt are added to the model initial conditions. The ring initially sits on the slope and is not completely balanced, as the thermal-wind assumption neglects the centrifugal force and the zero-velocity assumption on the sloping bottom

induces cross-shelf flow asymmetry. However, the ring adjusts itself dynamically in the first several days before the frontal subduction occurs (see below), and the details of the initial ring flow condition is not expected to alter the result here. To facilitate the perturbation growth, Gaussian random velocity perturbation with zero mean and standard deviation of 0.02 ms^{-1} is added to the ring current. Because this study focuses on the development of the ring-edge frontal subduction, all simulations are run for only 20 days (25 inertial periods), long enough to capture the shelf-water subduction phenomenon and the initial cross-shelfbreak offshore transport.

Three passive tracers, representing ring, shelf, and surface shelf waters with concentration C_r, C_s, and C_{s2}, respectively, are included in the model. The passive tracer equation is the same as the density equation except with no feedback to the circulation. The initial value of C_r is 1 in the WCR and 0 elsewhere (dashed magenta line in Fig. 2 represents the boundary). The initial value of C_s is 1 in the shelf water and 0 elsewhere with the boundary (dashed blue line in Fig. 2) aligning with a shelf water isopycnal. The initial concentration of C_{s2} is 1 in the top 50 m of the shelf onshore of y=–144 km and 0 elsewhere, and its boundary (dashed black-yellow line in Fig. 2) intercepts the isopycnal σ_θ= 26.3 kg m^{-3} (dashed black-red line in Fig. 2b). Note that C_s has no initial along-isopycnal variation and C_{s2} does. This difference has important dynamical consequence and help explain the cross-isopycnal characteristics of the subduction signal (Section 4). Sensitivity simulations (Table 1) with varying ring-water density ($\Delta\rho_0$), cross-shelf position of the ring (y_0) and spatially varying f ($f = f_0 + \beta y$) are also conducted.

3. Observational Analysis

3.1 General Pattern

SST in June 2014 shows the impingement of a WCR on the shelf edge (Fig. 1). On 02 June, the WCR is located to the southeast of the Pioneer Array moorings. It then migrates westward with its northwestern edge reaching the OS mooring on 08 June. In the next eight days, the northern edge of the ring migrates northward and reaches the OS mooring on 16 June. Meanwhile, a shelf-water streamer developed to the east of the ring with a cold (~18°C) patch transported offshore reaching 39.2°N on 25 June (Fig. 1d).

Time series data at both CO and OS moorings during the period of the ring impingement show episodic filaments with apparent downward signal propagation on the period of 1-2 days, as highlighted in Fig. 3. In particular, relatively cold (12-14°C), fresh (34-35.7 g kg^{-1}), high oxygen (>210 μmol kg^{-1}) and high CDOM signals descends underneath the relatively warm, saline, low oxygen and low CDOM ring water. Note that the apparent downward signal propagation does not necessarily represent downward water motion (see below). Also note that the high-frequency oscillations signals superposed on the descending signals mostly represent internal waves. The descending filaments appear on 13-14 and 18-19 June at the OS mooring (Fig. 3 left) and on 15-16 and 19-20 June at the CO mooring (Fig. 3 right). The filaments are ~20 m thick. During 13-14 June at the OS mooring and 15-16 June at the CO mooring, the filament signal propagates from z = –30 m to –110 m within a day. The corresponding vertical signal descending speed $|w_0| \approx 80$ m day^{-1} or 0.9 mm s^{-1}. The filament signal on 18-19 June at the OS mooring descends from z = –60 m to –120 m in two days with $|w_0| \approx 0.3$ mm s^{-1}. The signal on 19-20 June at the CO mooring descends from z = –40 m to –70 m in two days with $|w_0| \approx 0.2$ mm s^{-1}.

Physical and biogeochemical signatures of the filaments indicate that they represent diluted near-surface shelf water. The relatively low temperature and salinity of the water suggest that it originates from the outer shelf. In particular, the initial salinity of descending signal is <34.7 (Figs. 3b and 3g), so that at least part of the water in the filaments is from the onshore side of the shelfbreak front. The relatively high concentration of DO indicates that the filament shelf water has recently been exposed to the surface. The relatively high concentration of CDOM is consistent with the shelf origin of the filament water. Because of relatively high biological productivity, the MAB shelf water generally has higher concentration of DO and CDOM than the offshore waters (Vaillancourt et al. 2005). Consistently, the EB glider cross-shelf section shows a general trend of decreasing concentration of DO and CDOM toward offshore (Fig. 4c-d). Note that the CDOM concentration on the shelf also decreases slightly towards the surface, which is likely caused by photo-degradation (Fig. 4d).

Temperature-salinity (T-S) and oxygen-salinity (O-S) properties of the filament water suggest that the descending signals result from some type of downwelling flow. Because the filament water at the CO and OS moorings originates from the shelf side, it likely has passed through the CI mooring some time prior to reaching CO and OS moorings. Consistently, on the T-S and O-S diagrams, the deep filament waters at the CO and OS moorings overlap with the water at the CI mooring in May-June 2014 (Fig. 5). But the filament waters at the CO and OS moorings are located at greater depths than the water at the CI mooring of the same T-S and O-S properties. The depth differences suggest that the deep filament water at the CO and OS moorings has been transported downward after passing through the CI mooring.

291 Velocity data at the CO mooring (Fig. 6) indicate that the descending filaments
292 appear at the same time as the arrivals of the onshore edge of the WCR where the frontal
293 velocity starts to increase. Thus, the filaments likely represent a frontal process. A
294 barotropic northward onshore flow and a surface-intensified eastward along-shelf flow
295 appear on 15 June, approximately the same time as the first filament at the CO mooring
296 (cf. Fig. 3 right). As the ring edge near the moorings on 15-16 June is east-west oriented
297 (cf. Fig. 1c), the northward and the eastward flow represent a cross- and an along-front
298 current, respectively. The onshore flow lasts for a day with the maximum speed (after the
299 low-pass filter) of ~0.12 m s^{-1}. This onshore flow is presumably caused by the onshore
300 migration of the ring edge pushing the entire water column shoreward. The eastward flow
301 at the CO mooring persists for >6 days. During 16-17 June, the eastward (along-front)
302 flow occupies the entire water column. The maximum eastward speed in the raw and
303 low-pass filtered data is 1.22 and 0.48 m s^{-1}, respectively. This strong eastward flow
304 means that the shelfbreak flow is not two-dimensional (cross-shelf and vertical) and that
305 the observed filaments represent 3D slanted sheets of cold and fresh water being advected
306 eastward passing through the moorings by the ring-edge current. The measured cross-
307 shelf velocity at the mid-depth changes its direction to offshore on 16 June and remains
308 offshore for ~2 days. The filtered maximum offshore velocity of ~0.07 m s^{-1} occurs at
309 z=–50 m. This subsurface-intensified offshore velocity may represent a secondary flow
310 on the vertical section across the ring-edge front. However, no clear subsurface offshore
311 flow appears in the raw data. A similar but weaker pattern of cross-shelf velocity
312 variation exists on 18-20 June, coincident with the second filament at the CO mooring.

313 The EB glider cross-shelf transect on 02-04 June give a non-synoptic cross-
314 sectional view of the frontal feature (Fig. 4). It depicts the cross-shelf transition from the
315 ring water offshore to the shelf water onshore. The ring-edge isopycnals form a prograde
316 front at the shelf break. It shows an intermediate layer of low temperature, low salinity,
317 high DO and high CDOM shelf water extending offshore and downward underneath the
318 ring water, reaching z = –120 m, beyond the normal depth range of the shelf water. The
319 cross-shelf length scale of the intermediate shelf-water layer is ~10 km. This intermediate
320 layer is separated from the bottom by a 10-20 m thick bottom layer of low temperature,
321 intermediate salinity, low DO and low CDOM water. Consistent with the mooring data,
322 the temperature and salinity at the shelf end of the intermediate layer (at the 100-m
323 isobath) is ~12°C and <34.7 g kg^{-1}, respectively; salinity in the intermediate layer
324 increases gradually toward offshore. Other EB glider cross-shelf transects in the same
325 region at different times in June 2014 show qualitatively similar layering pattern (not
326 shown).
327 Data from the FZ glider along-shelf transect indicate that the frontal filament
328 feature likely occurs over an extended along-shelf distance on the onshore ring edge. The
329 CO mooring data show another descending filament on 23-25 June (Fig. 7 left). The cold,
330 fresh and high DO filament layer later rests at the depth of z = –80 m after 25 June with
331 much warmer and saltier water sitting above and slightly warmer and saltier water sitting
332 below. Meanwhile, the FZ glider along-shelf transect near the CO mooring on 25-28 June
333 show a ~20-m thick subsurface layer of relatively fresh (34-35.7 g kg^{-1}), cold (11-15°C)
334 and high CDOM shelf water spanning over the along-shelf distance of ~60 km (Fig. 7
335 right). This subsurface layer sits at the depth range of z = –60 - –80 m, below a surface

336 layer of ring water of high temperature (>22°C) and salinity (>36 g kg^{-1}) and above a
337 bottom layer of slope water of intermediate temperature (~16°C) and salinity (> 35.7 g
338 kg^{-1} and <36 g kg^{-1}). The middle layer presumably represents the filament water of
339 diluted shelf source captured by the CO mooring. Its along-shelf span suggests that the
340 filament likely extend in the along-shelf direction over a distance of >60 km, thus
341 forming a 3D sheet.

342 *3.2 Dynamics of the Frontal Filaments*

343 Based on their length and velocity scales, the observed frontal filaments represent
344 a submesoscale process. The unfiltered ring edge velocity U = 0.5-1 m s^{-1}; the cross-shelf
345 length scale of the subsurface shelf-water layer $L_c \approx$ 10 km; the thickness of the filaments
346 $H \approx$ 20 m; $N \approx 0.02$ s^{-1}; and $f = 9.37\times10^{-5}$ s^{-1}. Substituting these into (1) and (2) gives Ro
347 = 0.5-1 and Fr = 1-3, both $O(1)$. Substituting the vertical scale of the WCR in the slope
348 sea, H_r = 500 m, into (3) gives the first baroclinic Rossby radius of deformation of the
349 WCR in the slope sea, $L_R \approx$ 100 km. Therefore, $L_c < L_R$. All these satisfy the scaling for
350 submesoscale features (McWilliams 2016). As described in Section 1, two mechanisms
351 could potentially form the observed submesoscale frontal filaments: i) ageostrophic
352 frontal subduction and ii) horizontal stirring by geostrophic shear flow. Here, we discuss
353 the possibility of each process occurring at the ring edge.

354 Some of the filaments, except the one on 19-21 June at the CO mooring (Figs. 3
355 and 6), appear to be crossing isopycnals, differing from the classical pattern of along-
356 isopycnal frontal subduction (e.g., Spall 1995). The isopycnals over the filament periods
357 generally move downward but in a pace slower than the apparent filament descent.
358 Consequently, some of the filaments cross the isopycnals, and density (and salinity)

359 increases along the filaments. However, the filaments could still result from frontal
360 subduction, even though their cross-isopycnal characteristics do not fit the classical
361 pattern of frontal subduction. Other frontal processes could act on top of the frontal
362 subduction, modify the pattern, and result in the cross-isopycnal appearance. One
363 potential process is the mixing of the filament shelf water with the surrounding high
364 salinity water. To examine this, we compute time series of the vertical shear of horizontal
365 velocity, $\partial u/\partial z$ and $\partial v/\partial z$, at the CO mooring and the corresponding Richardson
366 Number,

367 $$Ri = \frac{N^2}{(\partial u/\partial z)^2 + (\partial v/\partial z)^2}. \quad (7)$$

368 The computation was done with raw *u* and *v* (Fig. 6e-f), and the *N* is interpolated onto the
369 same vertical 4-m grid as the velocity. It shows two bands of slightly elevated $\partial u/\partial z$,
370 low *Ri*, and presumably enhanced mixing on the top and bottom faces of the filament on
371 15-17 June. The enhanced vertical shear may be caused by the tidally-induced internal
372 waves in the region. However, the enhancement pattern is not distinct, and it remains
373 unclear whether mixing in the shelfbreak region is strong enough to modify the properties
374 of the filament water and result in the density variation along some of the filaments.
375 Another potential reason is that the observed filaments represent a subsurface 3D
376 cross-isopycnal sheet of shelf water being subducted at different isopycnals with different
377 temperature, salinity, DO and CDOM properties. This may occur because the tracer
378 contours in the MAB shelfbreak region often misalign with the isopycnals owing to the
379 great spiciness caused by the strong density compensation of temperature and salinity
380 (e.g., Todd et al. 2013; Zhang et al. 2011). The 3D shelf-water sheet could then be

advected though the moorings by the eastward frontal current and form the filaments with cross-isopycnal descending appearance (see Section 4 for more discussion on this).

Frontal geostrophic shear flow, as the other possibility of generating the tracer filaments, can intensify *existing* horizontal tracer gradients at depth through stirring, as described in (4), and forms a 3D, cross-isopycnal, tilted tracer sheet (Smith and Ferrari 2009). However, this purely geostrophic process would not induce vertical motion to transport the near-surface shelf water downward to the depth of the observed filaments. Other downward transport processes are required to establish the initial horizontal tracer gradients. Hence, regardless what causes the cross-isopycnal appearance of the filaments, the data suggests that some type of downwelling motion occurs at the ring edge. However, if the geostrophic shear stirring take place, the apparent signal descent observed at the moorings would be at least partially caused by the shear distortion, and the speed of the downward motion would be slower than the apparent descend rate.

Despite capturing the frontal filaments, the Pioneer Array measurements are not sufficient to resolve the temporal and spatial gradients associated with the filaments, which prevents the analysis of the submesoscale dynamics. The distance between the CO and OS moorings is 17.6 km, greater than the filament length scale. The time it takes a glider to cross the frontal region is about one day, which is similar to the filament development time scale. There were only one EB glider and one FZ glider in the region in June 2014, and they were over 30 km apart. In order to resolve the submesoscales, we use model simulations to examine the dynamics of the observed frontal filaments.

4. Modeling Analysis

4.1 General Pattern in the Model

SST from the ROMS control simulation shows surface deformation of the WCR (Fig. 8) in a pattern qualitatively similar to the structure observed in the satellite images (cf. Fig. 1). The ring and shelf waters come in direct contact on Day 9 as a limb of the WCR moving clockwise along the ring periphery reaches the 200-m isobath. At Day 10, some shelf water is pulled offshore of the 200-m isobath at $x \approx 50$ km. By Day 11, a prominent shelf-water streamer of 5-20 km wide has formed on the northeastern periphery of the WCR, and a cyclonic shelf-water ringlet is developed at the southeast end of the streamer, similar to observations (cf. Fig. 1d; Kennelly et al. 1985).

The model resolves the shelf-water frontal filaments at the northern ring edge with a pattern similar to the observed. The left column of Fig. 9 shows time series of various water-column properties at a fixed site near the ring-shelf water interface (triangles in Fig. 8c-f), which is comparable to the mooring data. It depicts clear descending signals of the shelf water tracer (C_s; Fig. 9a) and surface shelf water tracer (C_{s2}; Fig. 9b) at Day 10. The signals of both C_s and C_{s2} reaches $z = -220$ m on Day 11, much deeper than their respective initial depth range of $z > -80$ m and –50 m (Fig. 2). This thus indicates subduction of the shelf water at the ring edge.

The descending filaments of C_s and C_{s2} also differ from each other: the former is mostly along-isopycnal and the latter is steeper and crosses the isopycnal $\sigma_\theta = 26.3$ kg m^{-3} between $z = -100$ and –150 m (Fig. 9a-b). The former suggests that the subduction occurs within the same isopycnal interval, consistent with the classical pattern of frontal subduction. The cross-isopycnal appearance of the C_{s2} filament resembles some of the mooring-observed filaments. Note that the descending signal of C_s spans a isopycnal

427 range of σ_θ= 26.1-26.5 kg m^{-3} (Fig. 9a), and that C_s has no initial along-isopycnal
428 variation while C_{s2} does with the initial boundary intercepting the isopycnal σ_θ= 26.3 kg
429 m^{-3} (Fig. 2). The difference in the descending signals of C_s and C_{s2} thus suggests that the
430 cross-isopycnal appearance of the descending filament results from: i) subduction
431 transporting C_{s2}, including its cross-isopycnal boundary, in the isopycnal range of 26.1-
432 26.5 kg m^{-3} downward forming a 3D subsurface tracer layer, and ii) the advection of the
433 3D tracer layer passing through the 'mooring' generating the cross-isopycnal appearance
434 of the descending filament. Meanwhile, geostrophic shear stirring likely strains the
435 subsurface tracer layer and deforms the tracer boundary. This process could occur in the
436 real ocean as the density compensation between the temperature and salinity in the MAB
437 shelfbreak region causes temperature and salinity contours to intercept the density
438 contours with great spiciness (e.g., Todd et al. 2013). Because the model has no tidally-
439 induced internal waves to enhance mixing as in the real ocean, this explanation does not
440 necessarily preclude the possibilities of mixing contributing to the cross-isopycnal
441 appearance of observed filaments. As this study focuses on demonstrating the occurrence
442 of the frontal subduction, the detailed influence of these other factors on the subduction is
443 not investigated here.

444 Vertical cross-shelf section of the model field at Day 11 shows the initial
445 retrograde shelfbreak front (Fig. 2b) has been replaced by a prograde ring-edge front with
446 a clear subduction feature (Fig. 9 right), similar to the EB glider observations (Fig. 4). In
447 particular, an intermediate layer of shelf water resides underneath a surface of ring water
448 and a bottom layer of slope water. The shelf water is thus not in direct contact with the
449 bottom as it moves offshore, which is also consistent with the observations (e.g., Fig. 7).

The head of the shelf-water layer has moved offshore by 10 km and downward by 170 m. Cross-shelf section of the model velocity also shows a clear pattern of the subduction flow with offshore and downward velocity (Fig. 9k-l).

The model also shows that the subduction occurs over an along-shelf distance of several tens of kilometers. The vertically integrated C_s shows a substantial amount of shelf water underneath a surface layer of ring water on Day 10-12 (the blue area southwest of the green lines in Fig. 10b-d). On Day 10 the subduction layer spans an along-shelf distance of about 60 km, from x = 0 to 63 km; the along-shelf span expands to >100 km on Day 11.

4.2 Subduction Dynamics in the Model

The modeled ring edge velocity $U \approx 1$ m s^{-1}; the cross-shelf and vertical length scales of the subsurface shelf-water layer are $L_c \approx 10$ km and $H \approx 50$ m, respectively; $N \approx 0.01$ s^{-1}; and $f = 9.37\times10^{-5}$ s^{-1}. These together gives $Ro \approx 1$ and $Fr \approx 2$, both order-one. The modeled subduction feature is thus also a submesoscale phenomenon. To investigate the subduction dynamics, we calculate the divergence (δ), relative vorticity (ζ), stretch-strain deformation rate (S) of the modeled horizontal velocity, as well as the axial direction of the frontal principal flow deformation. We also perform the frontal tendency diagnosis following Capet et al. (2008a, 2008b) and Gula et al. (2014). The divergence, relative vorticity and stretch-strain rate are defined as

$$\delta = \frac{\partial u}{\partial x} + \frac{\partial v}{\partial y}, \tag{8}$$

$$\zeta = -\frac{\partial u}{\partial y} + \frac{\partial v}{\partial x}, \tag{9}$$

and

$$S = \left[\left(\frac{\partial u}{\partial x} - \frac{\partial v}{\partial y}\right)^2 + \left(\frac{\partial v}{\partial x} + \frac{\partial u}{\partial y}\right)^2\right]^{1/2}, \quad (10)$$

respectively. Note that (10) describes flow deformation due to both stretching and straining (Hoskins 1982). The direction of the principal flow deformation axis is described by the angle

$$\theta_p = \frac{1}{2}\tan^{-1}\left[\frac{(\partial v/\partial x) + (\partial u/\partial y)}{(\partial u/\partial x) - (\partial v/\partial y)}\right]. \quad (11)$$

The flow deformation is frontogenetic when the principal deformation axis aligns with the frontal axis, i.e., the angle between the two axes is $<\pi/4$ (Gula et al. 2014). The frontal tendency, T, is defined as the rate of change of the amplitude of the buoyancy gradient following a fluid parcel and satisfies,

$$T = \frac{1}{2}\frac{D\|\nabla b\|^2}{Dt} = T_{\mathrm{adv}} + T_w + T_{\mathrm{dv}} + T_{\mathrm{dh}}, \quad (12)$$

where,

$$T_{\mathrm{adv}} = \left(-\frac{\partial b}{\partial x}\nabla_h u - \frac{\partial b}{\partial y}\nabla_h v\right)\cdot\nabla_h b, \quad (13)$$

$$T_w = -\frac{\partial b}{\partial z}\nabla_h w \cdot \nabla_h b, \quad (14)$$

and

$$T_{\mathrm{dv}} = \nabla_h\left[\frac{\partial}{\partial z}\left(\kappa_\theta \frac{\partial b}{\partial z}\right)\right] w \cdot \nabla_h b \quad (15)$$

are the contributions of horizontal advection, vertical advection, and vertical mixing to the frontogenesis, respectively; and T_{dh} is the effect of the horizontal diffusion, which is implicit within the model numerical advection scheme in this study. In (12)-(15), $b = -g(\rho/\rho_0)$ is buoyancy, w is vertical velocity, κ_θ is vertical turbulent diffusivity, and $\nabla_h = (\partial x, \partial y, 0)$. A positive (negative) value of the right-hand-side terms in (12) means the

492 corresponding process is frontogenetic (frontolytic). T_{dh} is always frontolytic because the
493 numerical diffusion tends to smear the horizontal density gradient. As in Gula et al.
494 (2014), T_{dh} is generally secondary and thus neglected here.
495 The diagnostic quantities at $z = -3$ m and $t = 10$ days (Fig. 11) shows a peak of
496 front sharpness on the ring-shelf water interface west of $x = 63$ km with prominently
497 downward velocity, convergence (negative divergence), positive vorticity and large
498 stretch-strain rate. The principal deformation axis generally aligns with the axis of the
499 front. These are all characteristics of frontogenesis. The ring-shelf water interface east of
500 $x = 63$ km does not show a clear signal of frontogenesis. The frontal tendency diagnosis
501 shows that the horizontal flow advection strengthens the front in the region of
502 frontogenesis, while the vertical advection weakens the front. The effect of the vertical
503 mixing on the frontal strength is negative at the core of the front and positive to the
504 immediate southwest of the front.
505 A cross-front vertical section of the diagnostic quantities at Day 10 (Fig. 12)
506 shows that the frontogenesis pattern persists at depth. A stripe of elevated frontal
507 sharpness, convergence, positive relative vorticity and strong flow deformation aligns
508 with the ring-shelf water interface (the region of closely spaced black and grey lines in
509 Fig. 12). The frontal tendency diagnosis shows that effects of horizontal and vertical
510 advection at the front are positive and negative, respectively, and tends to balance each.
511 The influence of vertical mixing is negligible below the surface. These are all consistent
512 with the frontogenesis dynamics of filaments (double-sided fronts) in the Gulf Stream
513 (Gula et al. 2014). The cross-shelf alternating positive and negative vertical velocities
514 onshore of the front (Fig. 12d) and undulations of the isopycnals and C_s contour reflect

515 high-frequency internal waves excited at the front propagating onshore. Close
516 examination of the model solution indicates that these internal waves are generated by the
517 rapid onshore migration of the northern ring edge.

518 A region of negative vertical velocity of ~5km wide and 100 m thick is visible
519 below the ring-shelf water interface and offshore of $x = 0$ (inside the black frame in Fig.
520 12d). It reflects the subduction flow and generates the downward extending tongue of the
521 shelf water. A zoom-in view of the vertical and cross-frontal velocity in this frontal zone
522 show the subduction as a part of the cross-front secondary flow induced by the
523 frontogenesis (Fig. 13): An upwelling flow on the offshore side of the front transitions to
524 an onshore cross-frontal flow on the surface and then a downwelling flow on the onshore
525 side of the front.

526 All these confirm the occurrence of the 3D front subduction of the shelf water on
527 the onshore edge of the WCR. Essentially, as depicted in Fig. 14 schematically, the WCR
528 impinges on the shelf edge, and the cross-shelf density gradients on the onshore edge of
529 the ring intensifies. This frontogenesis causes flow straining and induces an ageostrophic
530 cross-front secondary circulation with strong vertical motion through potential vorticity
531 conservation (e.g., Capet et al. 2008a; Hoskins 1982; McWilliams et al. 2009; Spall
532 1995). Specifically, intensification of the frontal density gradient strengthens the frontal
533 jet and also vorticity on both sides of the jet (more negative on the light side and more
534 positive on the heavy side). Potential vorticity conservation then drives upwelling on the
535 light side of the front and downwelling on the heavy side of the front. An ageostrophic
536 cross-frontal surface flow from the light side towards the heavy side and a subsurface
537 compensating flow in the opposite direction develop. This secondary flow tends to relax

538 the steepening front. The downwelling velocity on the heavy side of the front and the
539 subsurface compensating flow together form the frontal subduction (Spall 1995). The
540 subducted water is then carried along the ring periphery away from the subduction site by
541 the frontal current, while the frontal subduction continues taking place on the onshore
542 ring edge as the ring keeps impinging on the shelf edge. The along-front extent of the
543 subduction is consistent with the along-front extent of frontogenesis, which is controlled
544 by the background convergent flow.

545 Close examination of the model solution show that this subduction process
546 actually occurs on the ring-slope water interface before the ring water is in contact with
547 the shelf water (Fig. 8a). That is, as the WCR starts to impinge on the shelf edge and the
548 ring edge front starts to intensify, the slope water that initially resides between the ring
549 and shelf waters is subducted and carried away. As the ring edge continues moving
550 shoreward, it comes into contact with the shelf water. Because the surface ring water is
551 less dense than the shelf water, the ring-edge density front persists, and the subduction
552 now transports the shelf water downward. The ring edge current then carries the
553 subducted shelf water into the slope sea. During this process, the initially retrograde front
554 at the shelf break is destroyed and replaced by the prograde density front, as indicated by
555 the orientation change of the isopycnals at 150-m water depth ($y = -150$ km) from Fig.
556 2b to Fig. 9g. Meanwhile, the surface cross-shelf density gradient, $\partial\rho/\partial y$, at $y = -150$
557 km has changed from its initial value of -0.6×10^{-4} kg m^{-4} to 6×10^{-4} kg m^{-4}.
558

559 **5. Discussion**

560 *5.1 Subduction Transport of the Shelf Water*

561 The model shows that the subducted shelf water underneath the surface ring water
562 is eventually transported offshore, providing a process of cross-shelfbreak offshore
563 transport of the shelf water that has no surface expression. The model demonstrates that
564 this subsurface transport of the shelf water occurs alongside of the surface-visible (to
565 satellites) shelf-water streamer (Fig. 10). This is consistent with field observations
566 sometimes showing subsurface shelf water adjacent to *surface-visible* shelf-water
567 streamers on the periphery of WCRs (e.g., Kupferman and Garfield 1977; Tang et al.
568 1985). From the prospective of someone who analyzes satellite remote-sensing data, the
569 subsurface offshore transport of the subducted shelf water thus behaves as a *surface-*
570 *invisible* part of the streamer transport.
571 Here we seek to qualitatively estimate the subduction-associated subsurface cross-
572 shelfbreak offshore transport (referred to as *surface-invisible*) of the shelf water in the
573 model and compare it to the *surface-visible* streamer transport. This separation is for a
574 practical purpose. As satellite data is often used to illustrate the shelf-water streamer in
575 the literature with an implicit assumption that the streamer transport is all visible on the
576 surface. Quantifying the surface-invisible part of the shelf water transport reveals the
577 amount of cross-shelfbreak offshore transport that is missed if one is to estimate the
578 overall transport based only on the surface information and some scaled depth (e.g.,
579 Bisagni 1983) or using a low-resolution model that does not resolve the subduction
580 process (e.g., Chen et al. 2014). To our knowledge, the surface-invisible offshore
581 transport the shelf water has not been specifically quantified in the literature, even though
582 it is included in the overall streamer transport of the shelf water in some studies (e.g.,
583 Cherian and Brink 2016).

584 Because the rapid evolution of the ring-shelf water interface hampers a direct
585 calculation of the shelf-water transport, we compute the transport indirectly from the
586 temporal change of the surface-visible and -invisible shelf water volume in the slope sea
587 (offshore of the 200-m isobath). The total volume of shelf water in the slope sea at time t
588 is computed using the shelf water passive tracer concentration, C_s, i.e.,

589 $$P_t(t) = \iiint_{V_{\text{offshore}}} C_s(t)dxdydz\,, \tag{16}$$

590 where V_{offshore} is the entire model volume offshore of the 200-m isobath. The separation
591 of the surface-visible and -invisible portions is based on the surface shelf-water
592 concentration, $C_s(x, y, 0)$. If $C_s(x, y, 0) > 0.1$, all shelf water within the water column
593 underneath $(x, y, 0)$ is considered surface-visible, and its domain-integrated volume in the
594 slope sea, P_v, is assumed to be the volume of shelf water that has been transported
595 offshore in the surface-visible streamer. The rest of the shelf water in the slope sea is
596 considered surface-invisible and has been transported offshore by the entrainment process
597 associated with the frontal subduction. Its domain-integrated volume in the slope sea is P_i
598 $= P_t - P_v$. The time rates of change of the volume quantities, $Q_t = \partial P_t/\partial t$, $Q_v = \partial P_v/\partial t$,
599 and $Q_i = \partial P_i/\partial t$, are calculated as the total, surface-visible and surface-invisible cross-
600 shelfbreak offshore transport of shelf water, respectively. Note that this approach
601 assumes i) only one continuous vertical layer of shelf water in the water column and ii)
602 no exchange of the two categories occurring offshore. It is very likely that these
603 assumptions do not hold in the real ocean, especially after a relatively long-period
604 evolution of the streamer in the slope sea. However, as this work focuses on the first
605 several days of the streamer evolution and the goal here is to provide a qualitative sense
606 on the baroclinic transport, the issues are not expected to severely affect the result.

607 Applying the separation approach to the control simulations shows that P_t, P_i and
608 P_v all increase over time in the 20-day simulation period (Fig. 15a). P_v starts to increase
609 slowly at Day 5, earlier than P_i. It is consistent with the shelf-water streamer developing
610 ahead of the shelf-water subduction (Fig. 10). Starting from Day 9, P_i starts to increase
611 rapidly and catches up with P_v at Day 14. After that, P_i saturates, while P_v continues
612 increasing. The saturation of P_i is caused by the cease of the frontogenesis and
613 subduction process as the ring limb (pointing northward in Fig. 8f) leaves the shallow
614 region. Overall, P_i and P_v are of the same order of magnitude. Correspondingly, Q_i
615 increases dramatically starting from Day 9 and reaches a peak of 0.8 Sv on Day 12,
616 representing 90% of the overall shelf-water cross-shelfbreak offshore transport at the
617 time (red lines in Fig. 15b-c). Over the 7-day period (Day 9-15) of shelf-water frontal
618 subduction, the mean surface-invisible offshore transport of the shelf water is ~0.4 Sv. It
619 is thus possible for the shelf-water offshore transport induced by the frontal subduction to
620 be a substantial transport relative to other mechanisms (e,g., PNI and surface visible
621 streamers).
622 Analysis of the satellite data over the period of 1979-1985 showed that WCR-
623 associated shelf-water streamers were present in the MAB region for ~70% of the time
624 (Garfield and Evans 1987). Assuming the subduction-induced subsurface transport occurs
625 over 1/4 of those times and all subduction events induces the shelf-water transport of 0.4
626 Sv, the same as in our control simulation, the surface-invisible offshore transport of the
627 shelf water averaged over all times would be ~0.07 Sv. This is significant relative to the
628 shelf-water offshore transport of 0.04-0.11 Sv required to balance the entire MAB
629 volume budget (Brink 1998). However, this is likely an overestimate as the simulations

630 presented in this study are based on a highly idealized model configuration of one
631 particular scenario. A more precise estimate of the subduction-induced shelf-water
632 offshore transport would require observations of higher spatial and temporal resolution or
633 realistic model simulations.

634 We here examine the dependence of modeled Q_i on the density anomaly of the
635 ring water ($\Delta\rho_0$, which is related to the strength of the ring), the initial cross-shelf
636 location of the WCR (y_0), and the spatial variation of f (Table 1). The simulations of
637 different $\Delta\rho_0$ show that when $|\Delta\rho_0| \leq 1$ kg m^{-3} Q_i increases with $|\Delta\rho_0|$ (Fig. 15b),
638 suggesting that intensity of the frontal subduction increases with the strength of the ring-
639 edge front. But, as $|\Delta\rho_0|$ increases from 1 to 1.25 kg m^{-3}, Q_i decreases slightly. The
640 simulations of different y_0 show that the subduction generally intensifies as the WCR gets
641 closer to the shelf break (Fig. 15d-e). The simulations with spatially varying f (β-plane)
642 show that the cross-shelf migration of the WCR resulted from the β-effect (Early et al.
643 2011) affects the subduction process (Fig. 15f-g). However, the relationships of Q_i with
644 $\Delta\rho_0$, y_0, and f are not linear. Closer examination of the model solutions shows that the
645 subduction intensity depends highly on the specific shape of the interface between the
646 ring and shelf waters. The ring-shelf water interface is strongly affected by the finite-
647 amplitude instability on the ring periphery. $\Delta\rho_0$, y_0, and f all exert strong influences on
648 the instability on the ring periphery. These influences and the development of the finite-
649 amplitude ring-edge instability are all nonlinear and might be related to the cross-frontal
650 difference in the potential vorticity. The detailed relationships between the subduction
651 process and those influencing factors and the underlying dynamics are left for future
652 studies.

653

654 *5.2 Comparison with the Open Ocean Process*

655 The basic dynamics of the frontal subduction described here is the same as the
656 submesoscale frontal processes previously studied in the open ocean environment.
657 Essentially, the frontal subduction is part of the cross-front secondary circulation that
658 tends to flatten the steepening front.

659 A major difference between the shelfbreak environment and the open ocean is the
660 presence of the shallow sloping bottom. It exerts strong influence on the evolution of the
661 WCR (e.g., Cherian and Brink 2016, 2018) and presumably causes the background
662 confluence flow on the ring edge that drives the frontal subduction. For the barotropic
663 offshore flow of the shelf water, the vertical stretching associated with the sloping bottom
664 is also important for the vorticity dynamics (Cherian and Brink 2018). However, the
665 subducted shelf water is separated from the bottom by a bottom layer of slope water
666 (Figs. 4 and 9), and the subduction layer of 20-50 m thick is relatively thin compared to
667 the water column of 100-200 m thick. Its dynamical evolution is thus less likely
668 influenced directly or altered qualitatively by the sloping bottom.

669 Because the MAB shelf break separates the shelf and slope/ring waters of
670 dramatically different physical and biogeochemical, the shelfbreak subduction process, as
671 a part of the cross-shelf transport, is potentially important. It could greatly affect the heat
672 and salt balance on the shelf, and export the outer shelf water that is rich in organic
673 matter into the deep part of the open ocean. The temperature and salinity differences
674 between the adjacent shelf and ring waters can reach 18°C and 3.5 g kg^{-1} (Zhang and
675 Gawarkiewicz 2015a). Meanwhile, density difference between the waters is generally <1

676 kg m^{-3}, as much of the density effects of temperature and salinity are compensatory. As
677 demonstrated in Section 3, the dramatic differences in the water properties provide a
678 great opportunity for visualizing the frontal subduction. The differences of the water
679 properties across a front in the open ocean are likely smaller, and the signal of frontal
680 subduction there is likely less visually dramatic.
681
682 *5.3 Potential Implication on Dynamics of Shelf-Water Streamer*
683 The potential influence of the frontal subduction on the shelf-water streamer is
684 considered here. We pose the hypothesis that the frontal subduction facilitates the
685 entrainment of the shelf water by the WCR and enhances the offshore streamer transport
686 of the shelf water.
687 The shelf-water subduction occurs on the shore side of the ring-edge front and
688 replaces the initially flat or retrograde isopycnals within a 5-10 km wide region next to
689 the ring-edge front with prograde isopycnals (Figs. 9g-l and 12a). Frontal subduction thus
690 spreads the prograde ring-edge front shoreward into the shelf water. This is consistent
691 with the EB glider transects showing the change of the shelf-water isopycnals at the 100-
692 m isobath from a retrograde tilt in the end of May before the ring impingement (not
693 shown) to a prograde tilt on 02-03 June after the ring impingement (Fig. 4a-b). Note that
694 the onshore edge of the ring has not yet reached the 100-m isobath on 02-03 June.
695 Through the thermal-wind balance, the prograde shelf-water isopycnals on 02-03 June
696 presumably enhances the eastward flow of the shelf water. This essentially represents a
697 baroclinically enhanced entrainment of the shelf water by the ring-edge current in a
698 narrow region at the outskirt of the ring edge. Presumably, the same baroclinic

699 mechanism applies to the ring edge to the eastern end of the ring-shelf contact region
700 where the baroclinically entrained shelf water would flow southeastward into the
701 streamer. The thermal-wind enhancement of the shelf-water entrainment by the prograde
702 front is consistent with the weaker cross-shelfbreak subsurface transport of the shelf
703 water in the sensitivity simulation of $|\Delta\rho_0| = 1.25$ kg m^{-3} (Fig. 15b). Compared to the
704 control case, the initial shelfbreak front in that case is weaker with smaller density
705 difference between the shelf and slope waters. Consequently, the prograde front at the
706 later stage is also weaker, which results in the weaker subsurface offshore transport of the
707 shelf water.

708 This subsurface baroclinic enhancement process is not included in the barotropic
709 mechanism of streamer formation proposed by Cherian and Brink (2016, 2018). Without
710 the shelf break front, their model shows that the outward sea level setdown of the ring
711 spreads onto the shelf as a barotropic influence and drives a geostrophic flow of the shelf
712 water. This barotropic shelf flow is ~40 km wide for the MAB scenario and named shelf-
713 water supply jet as it carries the shelf water along the ring periphery and into the slope
714 sea forming the shelf water streamer. The control simulation here shows a region of 30-
715 60 km wide north of the ring edge (enclosed by the blue contours in Fig. 8) where the
716 depth-averaged velocity changes from initially westward to eastward as the ring impinges
717 onto the shelf edge. This region presumably reflects the barotropic influence of the ring
718 on the shelf and corresponds to the barotropic shelf-water supply jet. Thus, in this model
719 the subduction-associated baroclinic transport takes place at the same time as the
720 barotropic transport and presumably enhances the cross-shelfbreak offshore transport of
721 the shelf water into the streamer. The baroclinic transport occurs over a region of only 5-

722 10 km wide, much narrower than the shelf region under the barotropic influence of the
723 ring, and is thus a part of the large-scale barotropic transport of the combined ring, slope
724 and shelf water on the upper-slope and outer-shelf.

725 To examine the temporal evolution of the streamer water volume before the
726 formation of the streamer, we use an adjoint tracer model (Zhang et al. 2010) starting
727 from the three-dimensional volume of the streamer on Day 12 (the white contour in Fig.
728 8f). The model simulates the backward tracer advection and diffusion of the shelf water.
729 The adjoint shelf-water tracer is then vertically integrated to obtain the shelf-water
730 thickness at each location and time. The 10-m thickness contours are used to outline the
731 locations of the streamer shelf water at the earlier times, i.e., the source regions (the white
732 lines in Fig. 8a-e). The result depicts the concurrence of the subduction-associated
733 subsurface transport and the surface-visible barotropic transport of the shelf water.

734 However, it remains unclear how the subduction-associated baroclinic process
735 would dynamically interact with the barotropic process and whether it is a separate
736 mechanism of forming the shelf-water streamer or merely an enhancement to the
737 barotropic mechanism. Another related question is where the streamer shelf water
738 originates on the shelf. The adjoint simulation indicates that, in this particular scenario
739 with the shelfbreak front, the streamer shelf water come from both east and west sides of
740 the streamer. However, whether this is generally true is a question to be explored in
741 future studies.

742

743 **6. Summary**

744 This study investigates the subduction of the MAB shelf water on the northern
745 edge of an impinging WCR as an enhancement to the transport of the shelf water into the
746 slope sea. This form of subduction-induced cross-shelfbreak offshore transport of the
747 shelf water at the shelf break occurs below the surface and does not have surface
748 signature. It explains historical observations of subsurface packets of shelf water in the
749 slope sea along the ring periphery whose formation mechanism was not specified in the
750 literature.

751 Analysis of the satellite and OOI Pioneer Array observations in the shelf break
752 region as well as an idealized numerical model simulation shows that the shelf-water
753 subduction is associated with the onshore impingement of the WCR and occurs when the
754 ring and shelf waters are in direct contact. Observations by the Pioneer Array moored
755 profilers in June 2014 show episodic filaments of diluted shelf water appearing
756 descending downward reaching depth beyond the normal depth range of shelf water. The
757 downward signal propagation coincides with the northern edge front of the WCR moving
758 through the moorings. A glider cross-shelf transect through the ring edge show a layer of
759 shelf water locating underneath the ring water. The model simulation reproduces the
760 basic pattern of shelf water subduction on the northern edge of an idealized WCR.

761 Both the Rossby and Froude numbers of the observed and modeled subduction are
762 order-one, meaning that the subduction is a submesoscale process, same as the frontal
763 subduction in the open ocean environment. Similar to the open ocean process, the
764 shelfbreak subduction on the northern edge of the WCR results from frontogenesis and is
765 a part of the cross-front secondary circulation that tends to relax the intensifying density
766 front. The subduction is a downwelling flow on the onshore side of the ring-edge front

767 and entrains the shelf water into the frontal region. The frontal current then carries the
768 subducted shelf water offshore underneath the ring water. Dynamics of the WCR-induced
769 shelf-water frontal subduction at the shelf break is the same as the frontal subduction in
770 the open ocean. However, the dramatically different physical and biogeochemical
771 properties of the shelf and ring waters at the shelf break provides a great opportunity to
772 visualize the subduction process.

773 The model also shows that the subducted shelf water is transported offshore
774 alongside of the surface-visible (to satellites) shelf water streamer. This strong connection
775 means that the subduction-induced subsurface cross-shelfbreak offshore transport of the
776 shelf water may be considered as a part of the shelf-water streamer. The model shows
777 that the surface-invisible offshore transport of the shelf water can be substantial relative
778 to the surface-visible streamer transport. The sensitivity simulations indicate that the
779 subduction-induced subsurface offshore transport of the shelf water varies strongly with
780 the density anomaly of the ring water, cross-shelf position of the ring and spatial
781 variation of the Coriolis parameter. To quantify the subsurface transport of the shelf
782 water associated with a particular WCR impingement event would require observations
783 of much higher spatial and temporal resolution or realistic high-resolution model
784 simulations.

785 We also propose that the frontogenesis-associated frontal subduction facilitates
786 the formation of the shelf-water streamer along the WCR periphery. The subduction-
787 associated downward flow results in onshore spreading of the prograde ring-edge density
788 front in a narrow region on the outskirt of the ring edge, which then enhances the
789 barotropic along-frontal flow of the shelf water in the region. This process likely

790 contributes to the entrainment of shelf water by the WCR and the formation of the shelf-
791 water streamer. How this baroclinic process interacts with the barotropic transport
792 remains to be investigated.

Acknowledgements

WGZ was supported by the National Science Foundation under grant OCE-1657853, OCE-1657803, and OCE 1634965. JP is grateful for the support of the Woods Hole Oceanographic Institution Summer Student Fellow Program in 2016 and 2017.

WGZ thanks Kenneth Brink, Glen Gawarkiewicz, Rocky Geyer, Steven Lentz, Dennis McGillicuddy, Robert Todd, and John Trowbridge for helpful discussions during the course of the study or useful comments on earlier versions of the manuscript.

The satellite sea surface temperature data was obtained from the University of Delaware Ocean Exploration, Remote Sensing, Biogeography Lab (led by Matthew Oliver) through the Mid-Atlantic Coastal Ocean Observing System (MARACOOS) data server (http://tds.maracoos.org/thredds/catalog.html). The OOI Pioneer Array mooring and glider data presented in this paper were download from the National Science Foundation OOI data portal (http://ooinet.oceanobservatories.org) in July-August 2016.

807 **References:**

808 Bisagni, J. J., 1983: Lagrangian current measurements within the eastern marin of a
809 warm-core Gulf Stream ring. *J. Phys. Oceanogr.*, **13,** 709-715.
810 Brink, K. H., 1998: Deep sea forcing and exchange processes. *The Global Coastal*
811 *Ocean: Process and Methods*, K. H. Brink, and A. R. Robinson, Eds., John Wiley and
812 Sons, 151-167.
813 Capet, X., J. C. McWilliams, M. J. Molemaker, and A. F. Shchepetkin, 2008a: Mesoscale
814 to submesoscale transition in the California Current System. Part I: Flow structure,
815 eddy flux, and observational tests. *J. Phys. Oceanogr.*, **38,** 29-42.
816 ——, 2008b: Mesoscale to submesoscale transition in the California Current System. Part
817 II: frontal processes. *J. Phys. Oceanogr.*, **38,** 44-64.
818 Chapman, D. C., and R. C. Beardsley, 1989: On the origin of shelf water in the Middle
819 Atlantic Bight. *J. Phys. Oceanogr.*, **19,** 384-391.
820 Chen, K., R. He, B. S. Powell, G. G. Gawarkiewicz, A. M. Moore, and H. G. Arango,
821 2014: Data assimilative modeling investigation of Gulf Stream Warm Core Ring
822 interaction with continental shelf and slope circulation. *Journal of Geophysical*
823 *Research - Oceans*, **119,** 5968–5991.
824 Cherian, D. A., and K. H. Brink, 2016: Offshore transport of shelf water by deep-ocean
825 eddies. *J. Phys. Oceanogr.*, **46,** 3599-3621.
826 ——, 2018: Shelf flows forced by deep-ocean anticyclonic eddies at the shelfbreak. *J.*
827 *Phys. Oceanogr.*, **48**, 1117-1138, doi: 10.1175/JPO-D-17-0237.1.

828 Churchill, J. H., P. C. Cornillon, and G. W. Milkowski, 1986: A cyclonic eddy and shelf-
829 slope water exchange associated with a Gulf Stream warm-core ring *J. Geophys. Res.*,
830 **91,** 9615-9623.
831 Early, J. J., R. M. Samelson, and D. B. Chelton, 2011: The evolution and propagation of
832 quasigeostrophic ocean eddies. *J. Phys. Oceanogr.*, **41,** 1535-1555.
833 Fratantoni, P., R. Pickart, D. Torres, and A. Scotti, 2001: Mean structure and dynamics of
834 the shelfbreak jet in the Middle Atlantic Bight during fall and winter. *J. Phys.*
835 *Oceanogr.*, **31,** 2135-2156.
836 Garfield, N., and D. L. Evans, 1987: Shelf water entrainment by Gulf Stream warm-core
837 rings. *J. Geophys. Res.*, **92,** 13003-13012.
838 Gawarkiewicz, G., F. Bahr, R. C. Beardsley, and K. H. Brink, 2001: Interaction of a slope
839 eddy with the shelfbreak front in the Middle Atlantic Bight. *J. Phys. Oceanogr.*, **21,**
840 2783-2796.
841 Gawarkiewicz, G., K. H. Brink, F. Bahr, R. C. Beardsley, M. Caruso, J. Lynch, and C.-S.
842 Chiu, 2004: A large-amplitude meander of the shelfbreak front in the Middle Atlantic
843 Bight: Observations from the Shelfbreak PRIMER Experiment. *Journal of*
844 *Geophysical Research - Oceans*, **109,** C03006.
845 Gawarkiewicz, G. G., and A. J. Plueddemann, 2018: Scientific rationale and conceptual
846 design in a process-oriented shelfbreak observatory: the OOI Pioneer Array. *Journal*
847 *of Operational Oceanography***,** sub judice.
848 Gawarkiewicz, G. G., C. A. Linder, J. F. Lynch, A. E. Newhall, and J. J. Bisagni, 1996:
849 A surface-trapped intrusion of slope water onto the continental shelf in the Mid-
850 Atlantic Bight. *Geophys. Res. Lett.*, **23,** 3763-3766.

851 Gula, J., M. J. Molemaker, and J. C. McWilliams, 2014: Submesoscale cold filaments in
852 the Gulf Stream. *J. Phys. Oceanogr.*, **44,** 2617-2643.
853 Hoskins, B. J., 1982: The mathematical theory of frontogenesis. *Annual Review of Fluid*
854 *Mechanics*, **14,** 131-152.
855 Houghton, R. W., F. Aikman III, and H. W. Ou, 1988: Shelf-slope frontal structure and
856 crossshelf exchange at the New England shelfbreak. *Cont. Shelf Res.*, **8,** 687-710.
857 Houghton, R. W., R. D. Vaillancourt, J. Marra, D. Hebert, and B. Hales, 2009: Cross-
858 shelf circulation and phytoplankton distribution at the summertime New England
859 shelfbreak front. *J. Mar. Syst.*, **78,** 411-425.
860 Joyce, T. M., 1991: Review of U. S. contribution to Warm-core rings. *Review of*
861 *Geophysics*, **Supplement (U.S. National Report to International Union of**
862 **Geodesy and Geophysics 1987-1990),** 610-616.
863 Joyce, T. M., J. K. B. Bishop, and O. B. Brown, 1992: Observations of offshore shelf-
864 water transport induced by a warm-core ring. *Deep Sea Research*, **39,** S97-S113.
865 Kennelly, M. A., R. H. Evans, and T. M. Joyce, 1985: Small-scale cyclones on the
866 periphery of the Gulf Stream warm-core ring. *J. Geophys. Res.*, **90,** 8845-8857.
867 Kupferman, S. L., and N. Garfield, 1977: Transport of low-salinity water at the slope
868 water-Gulf Stream boundary. *J. Geophys. Res.*, **82,** 3481-3486.
869 Lentz, S. J., 2003: A climatology of salty intrusions over the continental shelf from
870 Georges Bank to Cape Hatteras. *J. Geophys. Res.*, **108,** 24-21.
871 ——, 2008: Observations and a model of the mean circulation over the Middle Atlantic
872 Bight continental shelf. *J. Phys. Oceanogr.*, **38,** 1203-1221.

873 Levy, M., P. Klein, and A.-M. Treguier, 2001: Impact of sub-mesoscale physics on
874 production and subduction of phytoplankton in an oligotrophic regime. *J. Mar. Res.*,
875 **59,** 535-565.
876 Linder, C. A., and G. G. Gawarkiewicz, 1998: A climatology of the shelfbreak front in
877 the Middle Atlantic Bight. *J. Geophys. Res.*, **103,** 18,405-418,423.
878 Mahadevan, A., and A. Tandon, 2006: An analysis of mechanisms for submesoscale
879 vertical motion at ocean fronts. *Ocean Model.*, **14,** 241-256.
880 McDougall, T. J., D. R. Jackett, F. J. Millero, R. Pawlowicz, and P. Barker, 2012: A
881 global algorithm for estimating Absolute Salinity. *Ocean Sci.*, **8,** 1123-1134.
882 McWilliams, J. C., 2016: Submesoscale currents in the ocean. *Proceedings of the Royal*
883 *Society A*, **472,** 20160117.
884 McWilliams, J. C., M. J. Molemaker, and E. I. Olafsdottir, 2009: Line fluctuation growth
885 during frontogenesis. *J. Phys. Oceanogr.*, **39,** 3111-3129.
886 Omand, M. M., E. A. D'Asaro, C. M. Lee, M. J. Perry, N. Briggs, I. Cetinie, and A.
887 Mahadevan, 2015: Eddy-driven subduction exports particulate organic carbon from
888 the spring bloom. *Science*, **348,** 222-225.
889 Schlitz, R., 2003: Interaction of shelf water with warm-core rings, focusing on the
890 kinematics and statistics of shelf water entrained within streamers. NOAA Technical
891 Memorandum NMFS-NE-170, 46 pp.
892 Shchepetkin, A. F., and J. C. McWilliams, 2008: Computational kernel algorithms for
893 fine-scale, multiprocess, long-term oceanic simulations. *Handbook of Numerical*
894 *Analysis. XIV: Computational Methods for the Atmosphere and the Ocean*, P. G.
895 Ciarlet, R. Temam, and J. Tribbia, Eds., Elsevier Science, 121-183.

896 Smith, K. S., and R. Ferrari, 2009: The production and dissipation of compensated
897 thermohaline variance by mesoscale stirring. *J. Phys. Oceanogr.*, **39,** 2477-2501.
898 Spall, M. A., 1995: Frontogenesis, subduction, and cross-front exchange at upper ocean
899 fronts. *J. Geophys. Res.*, **100,** 2543-2557.
900 Tang, C. L., A. S. Bennett, and D. J. Lawrence, 1985: Thermohaline intrusions in the
901 frontal zones of a warm-core ring observed by Batfish. *J. Geophys. Res.*, **90,** 8928-
902 8942.
903 Todd, R. E., G. G. Gawarkiewicz, and W. B. Owens, 2013: Horizontal scales of
904 variability over the Middle Atlantic Bight shelfbreak and continental rise from
905 finescale observations. *J. Phys. Oceanogr.*, **43,** 222-230.
906 Vaillancourt, R. D., J. Marra, L. Prieto, R. W. Houghton, B. Hales, and D. Hebert, 2005:
907 Light absorption and scattering by particles and CDOM at the New England
908 shelfbreak front. *Geochem., Geophys., Geosyst.*, **6,** Q11003.
909 Warner, J. C., C. R. Sherwood, H. G. Arango, and R. P. Signell, 2005: Performance of
910 four turbulence closure models implemented using a generic length scale method.
911 *Ocean Model.*, **8,** 81-113.
912 Zhang, W. G., and G. G. Gawarkiewicz, 2015a: Dynamics of the Direct Intrusion of Gulf
913 Stream Ring Water onto the Mid-Atlantic Bight Shelf. *Geophys. Res. Lett.*, **42,** 7687-
914 7695.
915 ——, 2015b: Length-scale of the finite-amplitude meanders of shelfbreak fronts. *J. Phys.*
916 *Oceanogr.*, **45,** 2598-2620.
917 Zhang, W. G., J. L. Wilkin, and O. M. E. Schofield, 2010: Simulation of water age and
918 residence time in New York Bight. *J. Phys. Oceanogr.*, **40,** 965-982.

919 Zhang, W. G., G. G. Gawarkiewicz, D. J. McGillicuddy, and J. L. Wilkin, 2011:
920 Climatological mean circulation at the New England shelf break. *J. Phys. Oceanogr.*,
921 **41,** 1874-1893.
922

Figure Captions:

Fig. 1. Satellite-measured SST in the northern Mid-Atlantic Bight region at four different times in June 2016. The white areas represent cloud cover. The thin black lines are isobath contours. The diamonds indicate locations of the OOI Pioneer Array moorings with the green, black and blue filled ones representing the Offshore, Central Offshore and Central Inshore moorings, respectively; the thick white line in (a) is the track of the EB glider transect shown in Fig. 4; The thick white line in (d) is the track of the FZ glider transect shown in Fig. 7 right column. The triangles and squares represent the beginning and end of the transects, respectively.

Fig. 2. Model initial density (color) and velocity (vectors in (a) and black contours in (b)) fields on the (a) surface and (b) the cross-shelf section going through the center of the warm-core ring (the dashed black line in (a)). The velocity scale is provided at the top-right corner of (a). The dashed blue, black-yellow and magenta lines are the edges of the shelf (C_s), surface-shelf (C_{s2}) and warm-core ring (C_r) waters, respectively. The dashed black-red line in (b) highlights the isopycnal of 26.3 kg m^{-3} on the shelf, which intercepts the boundary of C_{s2} (the dashed black-yellow line). The grey lines in (a) are isobath contours. Note that the thermal-wind-balanced, westward, initial shelfbreak front jet exists throughout the along-shelf extent of the model domain. It does not show up on the velocity contour in (b) because it is weakened in the central region of the domain ($x \in$(–40, 40 km)) by the subsurface prograde isopycnal tilt associated with the ring.

946 Fig. 3. Temporal evolution of potential temperature, absolute salinity, DO, and CDOM
947 concentration vertical profile measured at the (left) Offshore and (right) Central Offshore
948 moorings on 13-21 June 2014. The solid lines in each panel are isopycnals with the
949 contour interval of 0.5 kg m^{-3}. The dashed lines highlight the descending signals
950 described in the text.
951
952 Fig. 4. Cross-shelf section of potential temperature, absolute salinity, DO and CDOM
953 measured by a Pioneer Array EB glider over 2-4 June 2014. The thin lines in each panel
954 are isopycnals with the contour interval of 0.5 kg m^{-3}. The thick grey lines are the bottom.
955 The tracks of the glider missions are shown in Fig. 1a. The dashed lines highlight the
956 subsurface layer of shelf water described in the text.
957
958 Fig. 5. (Top) Temperature-salinity and (bottom) Oxygen-salinity diagrams of the data
959 measured by the Offshore (black-circled dots in the left column), Central Offshore
960 (black-circled dots in the right column) and Central Inshore (small colored dots with no
961 circles in both columns) mooring profilers. The color of the dots represents the depth of
962 the measurements. For the Offshore mooring, only the data in the descending filaments
963 on 13-14 June 2014 below $z = -70$ m (Fig. 3 left) is shown; For the Central Offshore
964 mooring, only the data in the descending filament on 15-17 June 2014 below $z = -70$ m
965 (Fig. 3 right) is shown; For the Central Inshore mooring, data at all depth within the
966 period of 01 May – 21 June 2014 are shown.
967

968 Fig. 6. Time series of (left) raw and (right) low-pass filtered (a-b) u, (c-d) v, (e-f) $\partial u/\partial z$,
969 and (g) Richardson number at the Central Offshore mooring on 13-21 June, 2014. The
970 thin black lines are isopycnals with the interval of 0.5 kg m^{-3}; the white dashed lines
971 corresponding to the descending signals in the mooring CTD data (Fig. 3 right column);
972 the green ellipses in (e) and (f) highlight the region of slightly enhanced mixing.
973
974 Fig. 7. (left) Time series of potential temperature, absolute salinity, and DO measured by
975 the CO mooring over 22-28 June, 2014; (right) along-shelf section of temperature,
976 salinity, and CDOM measured by a Pioneer Array FZ glider over 25-28 June 2014 with
977 the track shown in Fig. 1d. The thin solid lines in each panel are isopycnals with the
978 contour internal of 0.5 kg m^{-3}. The dashed lines in the left panels highlight the descending
979 signal. The grey thick lines are the bottom. The mooring CDOM and glider DO data are
980 not shown because of bad data.
981
982 Fig. 8. Snapshots of the model surface density (color) and velocity (vectors) at different
983 times. The black lines are the contour of 50% shelf water concentration; The thin blue
984 lines are the contours of zero vertically-averaged along-shelf current on the shelf,
985 outlining the shelf region under barotropic influence of the ring; The thick white lines
986 depict the source region of the Day-12 streamer shelf water at different times obtained
987 from the adjoint simulation; The triangles in (c-f) indicate the location of the model time
988 series shown in Fig. 9 left column; The blue-white dashed line in (e) indicates the cross-
989 shelf transect shown in Fig. 9 right column; The boxes in (d-f) depicts the area of view in

990 Fig. 10; the grey dashed lines are isobath contours; 'IP' in each panel represents inertial
991 period.
992
993 Fig. 9. (left) Time series of modeled (a) shelf water concentration (C_s), (b) surface shelf
994 water concentration (C_{s2}), (c) ring water concentration (C_r), (d) eastward velocity, (e)
995 northward velocity, and (f) vertical velocity at a fixed location (triangles in Fig. 8c-f)
996 over the period of frontal subduction; (right) a cross-frontal transect of the same variables
997 at x = 47 km and t = 11 days (blue dashed line in Fig. 8e). The black curves in all panels
998 are contours of σ_θ with the interval of 0.2 kg m^{-3} and the 26.3 kg m^{-3} contour highlighted
999 in bold. The dashed white lines in (a) and (g) highlight the subduction signals of the shelf
1000 water; the dashed green lines in (b) and (h) highlight the subduction signals of the surface
1001 shelf water; dashed yellow lines in (g), (h) and (i) represent the edges of the shelf,
1002 surface-shelf and ring waters, respectively, in the initial conditions.
1003
1004 Fig. 10. Snapshots of vertically integrated shelf water concentration (i.e., the effective
1005 thickness of the shelf water; color) and contours of shelf water concentration C_s = 0.1
1006 (red lines), 0.5 (green lines) and 0.75 (yellow lines) on sea surface. The vectors indicate
1007 the surface velocity with the scale at the top-left corner of (a), and the grey dashed lines
1008 are isobath contours. The box in (b) indicate the area of view in Fig. 11.
1009
1010 Fig. 11. Horizontal distribution of (a) frontal sharpness, (b) vertical velocity, (c)
1011 divergence, (d) relative vorticity, (e) stretch-strain rate (color) and principal deformation
1012 axis (thick blue lines), as well as the frontogenesis tendency terms due to (f) horizontal

1013 advection, (g) vertical advection, and (h) vertical mixing at z = –3 m and t = 10 days in a
1014 frontal region (black box in Fig. 10b). The dashed green lines are the contour of C_s (x, y,
1015 0) = 0.5, indicating the location of the ring-edge front; The arrows are vectors of the
1016 surface velocity; The triangles in (a) and (b) indicate the location of the model time series
1017 in Fig. 9 left column; The dashed black-magenta lines in (a) and (b) indicate the location
1018 of the cross-frontal section in Fig. 12; The grey dashed lines are isobath contours.
1019
1020 Fig. 12. Cross-frontal section of (a) σ_θ, (b) eastward velocity, (c) frontal sharpness, (d)
1021 vertical velocity, (e) divergence, (f) relative vorticity, (g) stretch-strain rate, as well as the
1022 frontogenesis tendency terms due to (h) horizontal advection, (i) vertical advection, and
1023 (j) vertical mixing along a line normal to the front (magenta lines in Fig. 11a-b) at t = 10
1024 days. The black lines are the contours of C_s = 0.5, and the grey lines are the contours of
1025 C_r = 0.5. The boxes in (a) and (d) indicate the zoom-in region shown in Fig. 13.
1026
1027 Fig. 13. A zoom-in view of the density (color) and secondary circulation (v_f and w;
1028 vectors) on the cross-frontal section (see the boxes in Figs. 12a and 12d for the area of
1029 view). Here, v_f is horizontal velocity in the cross-frontal direction. The scales of v_f and w
1030 are shown on the top-right corner. The black and grey lines is the contours of the shelf
1031 and ring water concentration of 0.5, respectively.
1032
1033 Fig. 14. A schematic of the 3D frontal subduction processes at the northern edge of the
1034 impinging warm-core ring. The big red arrow indicates the onshore migration of the
1035 WCR; the solid red lines represent two ring-edge isopycnals on the surface; the dashed

1036 red lines represent two ring-edge isopycnals on the vertical cross-shelf section; the thin
1037 black arrows represent the frontal jet on the surface. The blue, thick black and dashed
1038 green arrows depicts the secondary flow on a cross-frontal vertical section: the solid blue
1039 arrow indicates the subduction flow on the heavy side of the front; the thick black arrow
1040 indicates the cross-frontal onshore flow on the surface; the dashed green arrow indicates
1041 the upward flow on the light side of the front.
1042
1043 Fig. 15. Time series of modeled (a) volume of shelf water in the slope sea (offshore of the
1044 200-m isobath), (b, d and f) surface-invisible offshore transport of the shelf water, and (c,
1045 e and g) fraction of the total offshore shelf water transport being surface invisible. The
1046 results in (a) are obtained from the control simulation; those in (b-c) are from sensitivity
1047 simulations of different ring water density anomaly ($\Delta\rho_0$); those in (d-e) are from
1048 sensitivity simulations of different initial cross-shelf position of the ring (y_0); and those in
1049 (f-g) are from sensitivity simulations of different β. The red curves in (b-g) are obtained
1050 from the control simulation. In (c), (e) and (g) only the faction at times of the total
1051 offshore shelf water transport exceeding 0.02 Sv is shown.
1052

1053 **Table 1. Model Sensitivity Parameters**

Symbol	Sensitivity parameter	Unit	Values[a]
$\Delta\rho_0$	Surface density anomaly of the ring water	kg m^{-3}	–0.5; –0.75; **–1**; –1.25
y_0	Cross-shelf location of the ring center	km	–240; **–245**; –250; –255
β	Northward gradient of Coriolis Parameter ($\partial f/\partial y$)	10^{-11} $(m\ s)^{-1}$	–1.76; **0**; 1.76

1054

1055 [a]The control values of the parameters are highlighted in bold.

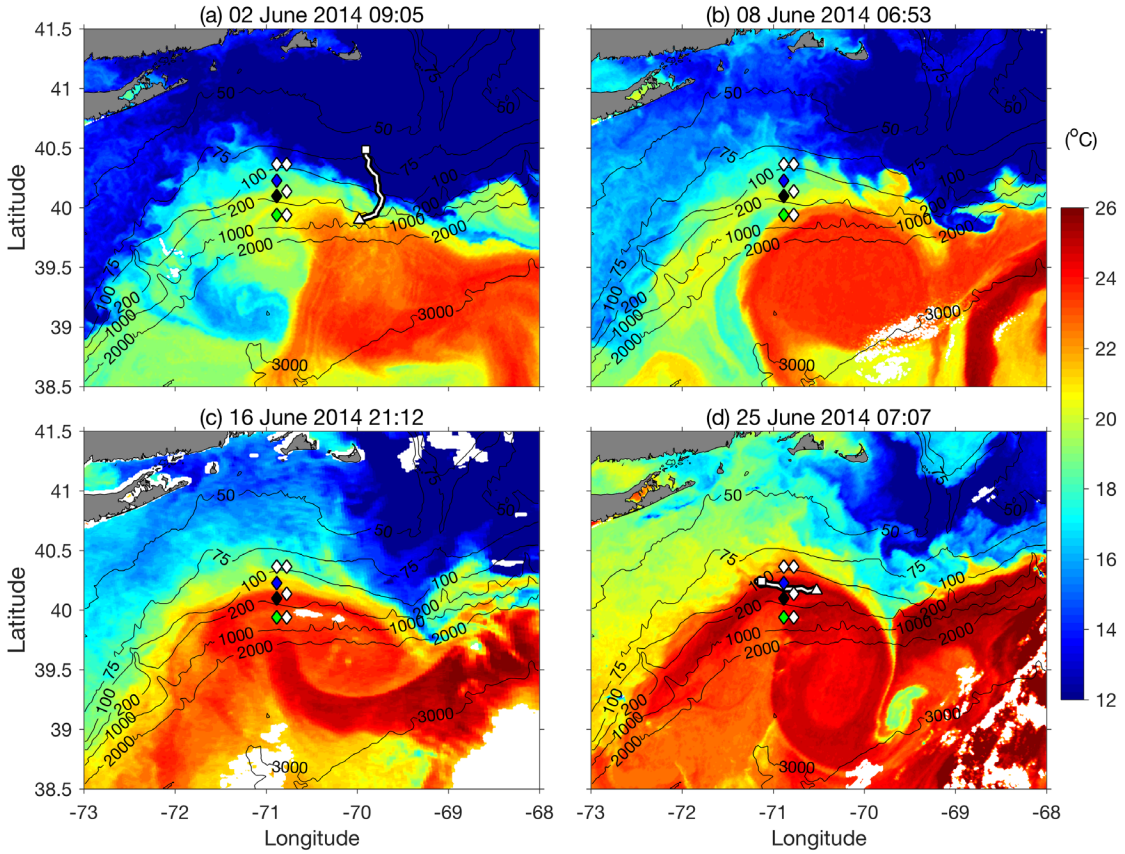

Fig. 1. Satellite-measured SST in the northern Mid-Atlantic Bight region at four different times in June 2016. The white areas represent cloud cover. The thin black lines are isobath contours. The diamonds indicate locations of the OOI Pioneer Array moorings with the green, black and blue filled ones representing the Offshore, Central Offshore and Central Inshore moorings, respectively; the thick white line in (a) is the track of the EB glider transect shown in Fig. 4; The thick white line in (d) is the track of the FZ glider transect shown in Fig. 7 right column. The triangles and squares represent the beginning and end of the transects, respectively.

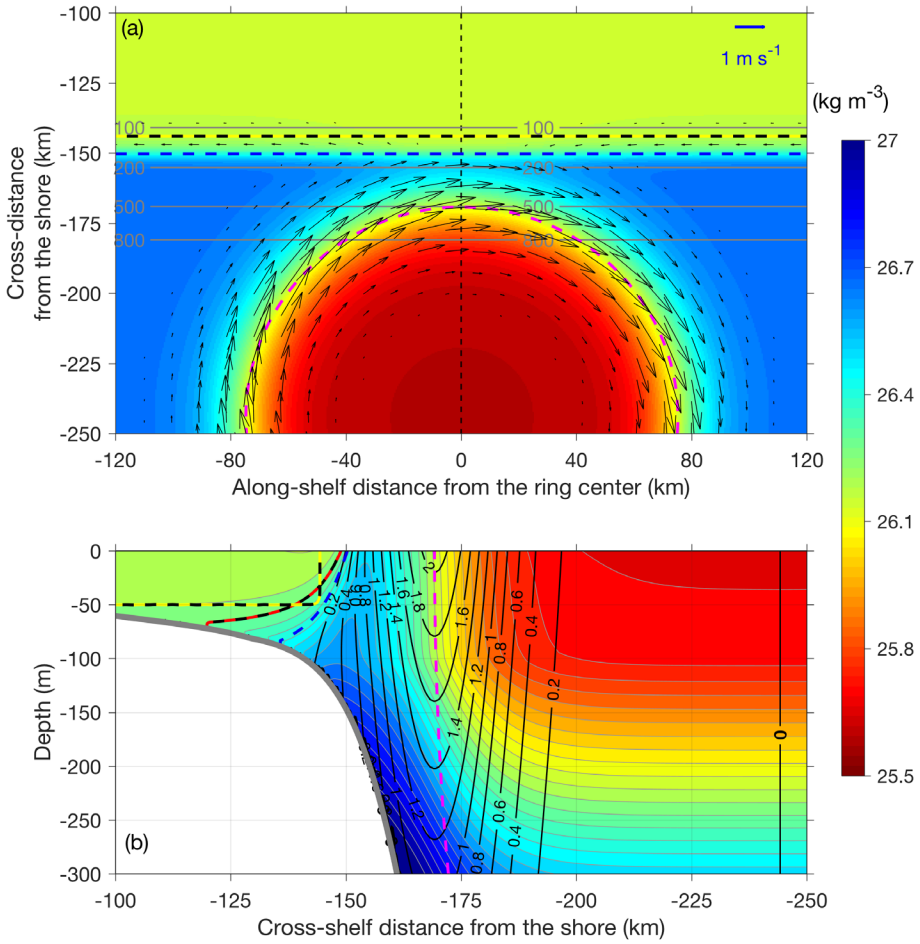

Fig. 2. Model initial density (color) and velocity (vectors in (a) and black contours in (b)) fields on the (a) surface and (b) the cross-shelf section going through the center of the warm-core ring (the dashed black line in (a)). The velocity scale is provided at the top-right corner of (a). The dashed blue, black-yellow and magenta lines are the edges of the shelf (C_s), surface-shelf (C_{s2}) and warm-core ring (C_r) waters, respectively. The dashed black-red line in (b) highlights the isopycnal of 26.3 kg m^{-3} on the shelf, which intercepts the boundary of C_{s2} (the dashed black-yellow line). The grey lines in (a) are isobath contours. Note that the thermal-wind-balanced, westward, initial shelfbreak front jet exists throughout the along-shelf extent of the model domain. It does not show up on the velocity contour in (b) because it is weakened in the central region of the domain ($x \in (-40, 40$ km)) by the subsurface prograde isopycnal tilt associated with the ring.

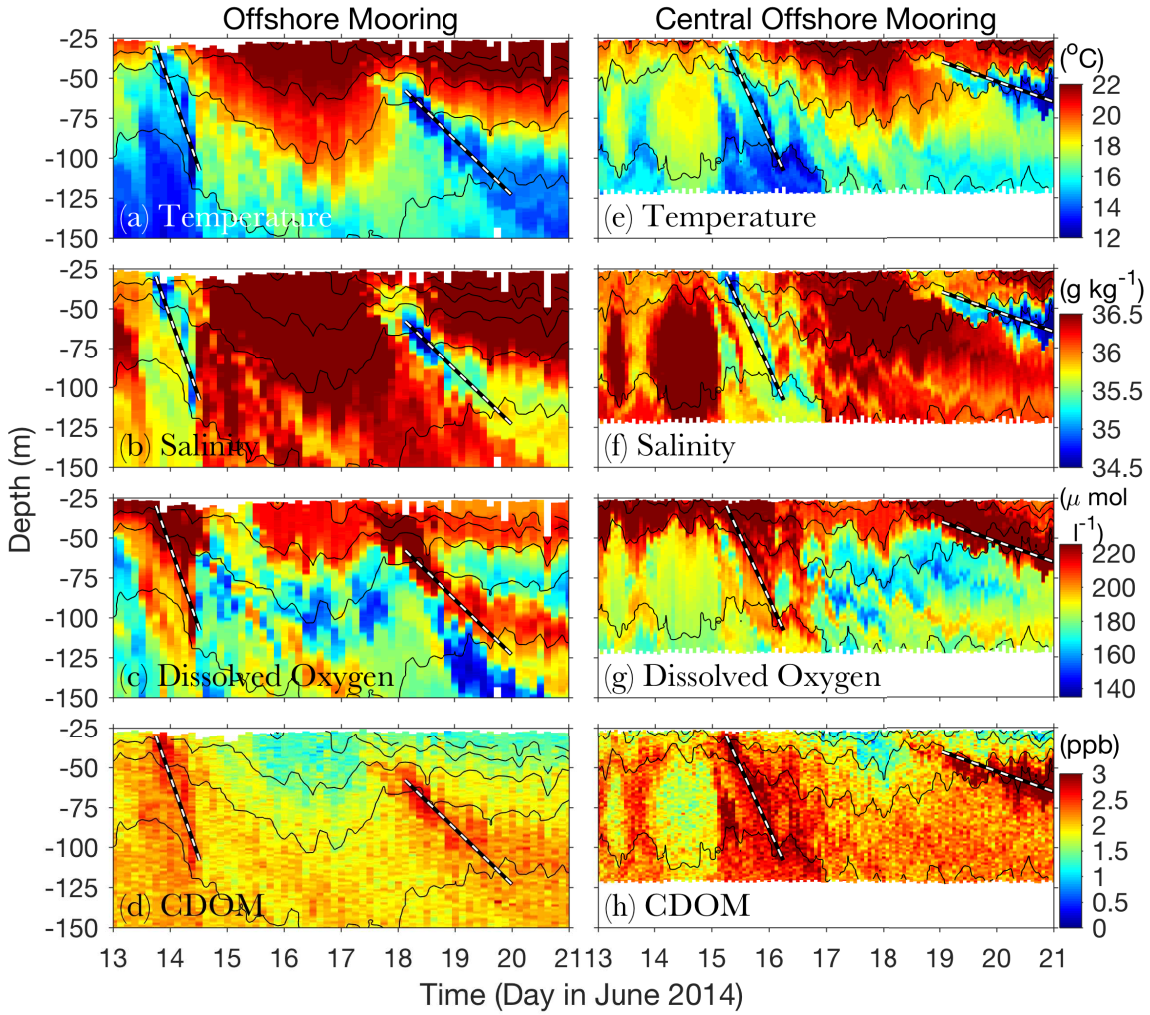

Fig. 3. Temporal evolution of potential temperature, absolute salinity, DO, and CDOM concentration vertical profile measured at the (left) Offshore and (right) Central Offshore moorings on 13-21 June 2014. The solid lines in each panel are isopycnals with the contour interval of 0.5 kg m^{-3}. The dashed lines highlight the descending signals described in the text.

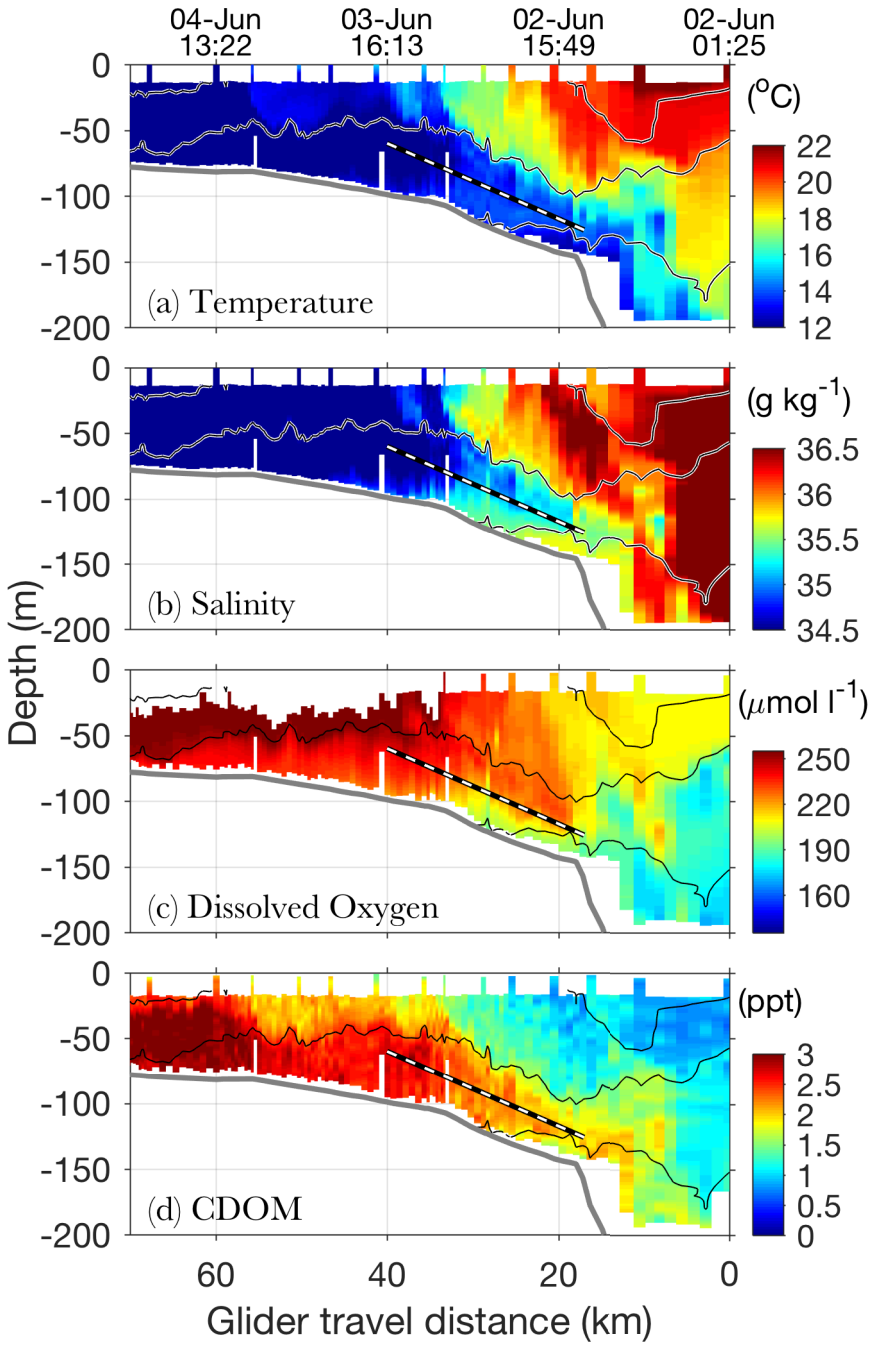

Fig. 4. Cross-shelf section of potential temperature, absolute salinity, DO and CDOM measured by a Pioneer Array EB glider over 2-4 June 2014. The thin lines in each panel are isopycnals with the contour interval of 0.5 kg m^{-3}. The thick grey lines are the bottom. The tracks of the glider missions are shown in Fig. 1a. The dashed lines highlight the subsurface layer of shelf water described in the text.

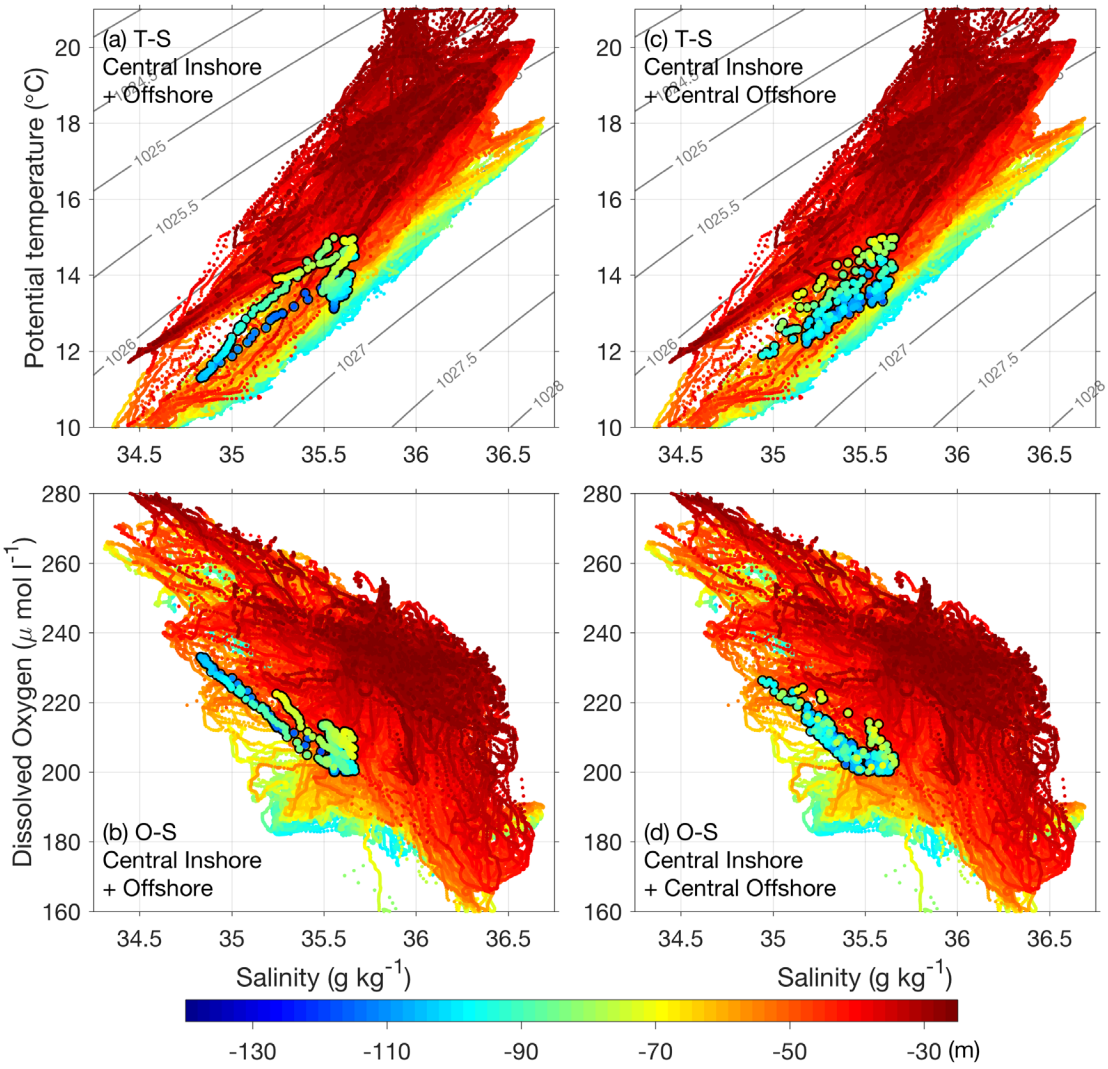

Fig. 5. (Top) Temperature-salinity and (bottom) Oxygen-salinity diagrams of the data measured by the Offshore (black-circled dots in the left column), Central Offshore (black-circled dots in the right column) and Central Inshore (small colored dots with no circles in both columns) mooring profilers. The color of the dots represents the depth of the measurements. For the Offshore mooring, only the data in the descending filaments on 13-14 June 2014 below $z = -70$ m (Fig. 3 left) is shown; For the Central Offshore mooring, only the data in the descending filament on 15-17 June 2014 below $z = -70$ m (Fig. 3 right) is shown; For the Central Inshore mooring, data at all depth within the period of 01 May – 21 June 2014 are shown.

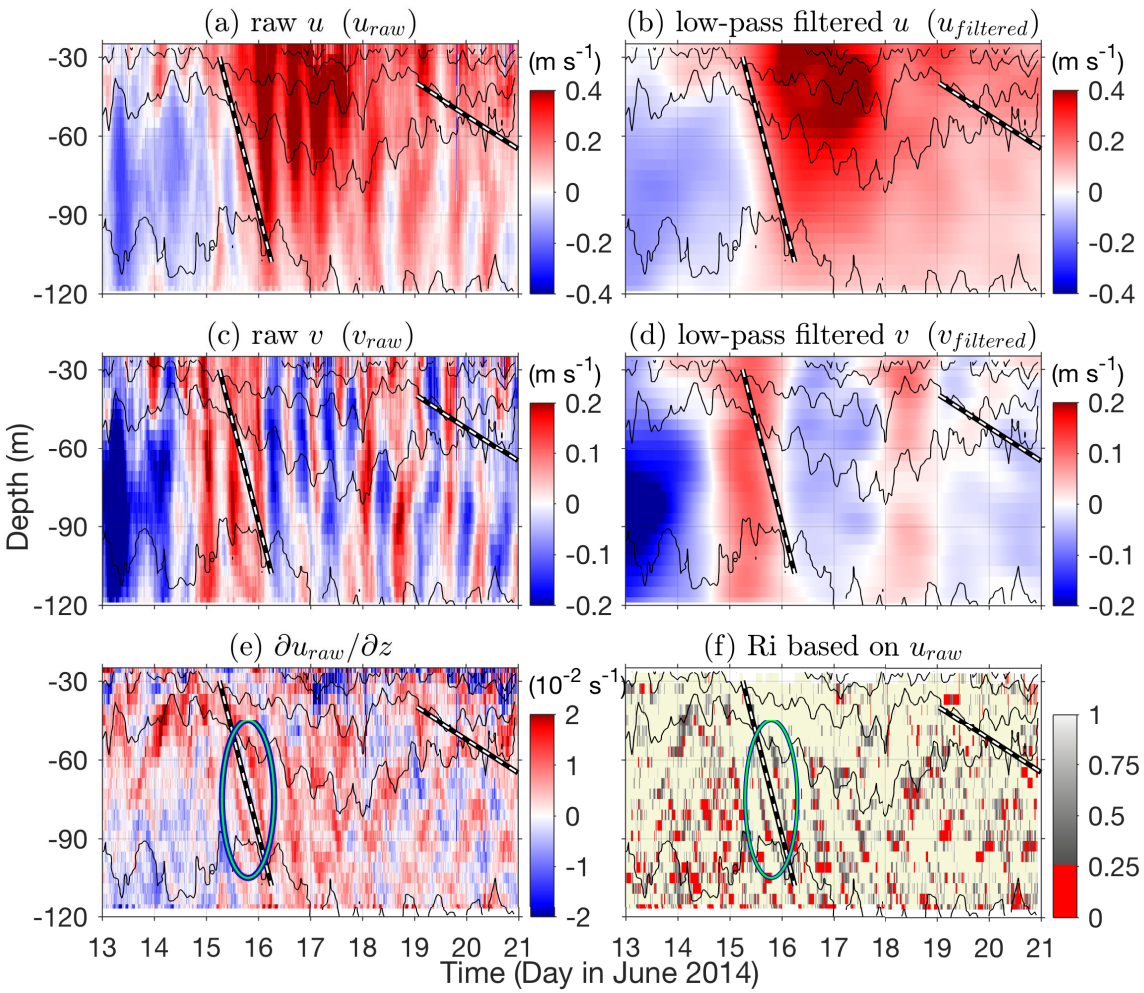

Fig. 6. Time series of (left) raw and (right) low-pass filtered (a-b) u, (c-d) v, (e-f) $\partial u/\partial z$, and (g) Richardson number at the Central Offshore mooring on 13-21 June, 2014. The thin black lines are isopycnals with the interval of 0.5 kg m^{-3}; the white dashed lines corresponding to the descending signals in the mooring CTD data (Fig. 3 right column); the green ellipses in (e) and (f) highlight the region of slightly enhanced mixing.

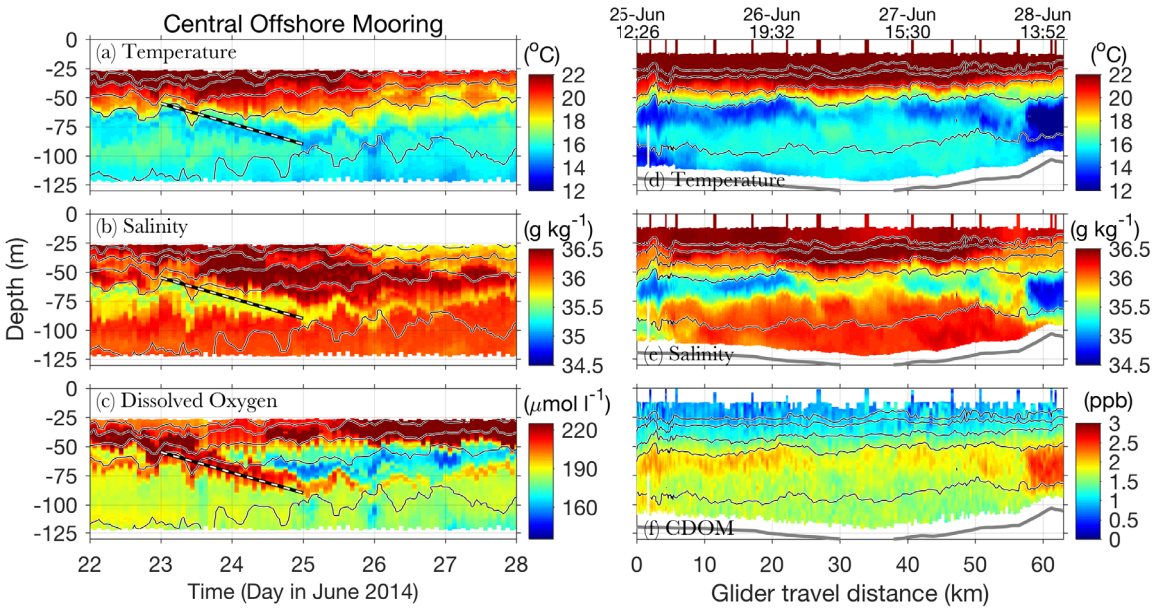

Fig. 7. (left) Time series of potential temperature, absolute salinity, and DO measured by the CO mooring over 22-28 June, 2014; (right) along-shelf section of temperature, salinity, and CDOM measured by a Pioneer Array FZ glider over 25-28 June 2014 with the track shown in Fig. 1d. The thin solid lines in each panel are isopycnals with the contour internal of 0.5 kg m^{-3}. The dashed lines in the left panels highlight the descending signal. The grey thick lines are the bottom. The mooring CDOM and glider DO data are not shown because of bad data.

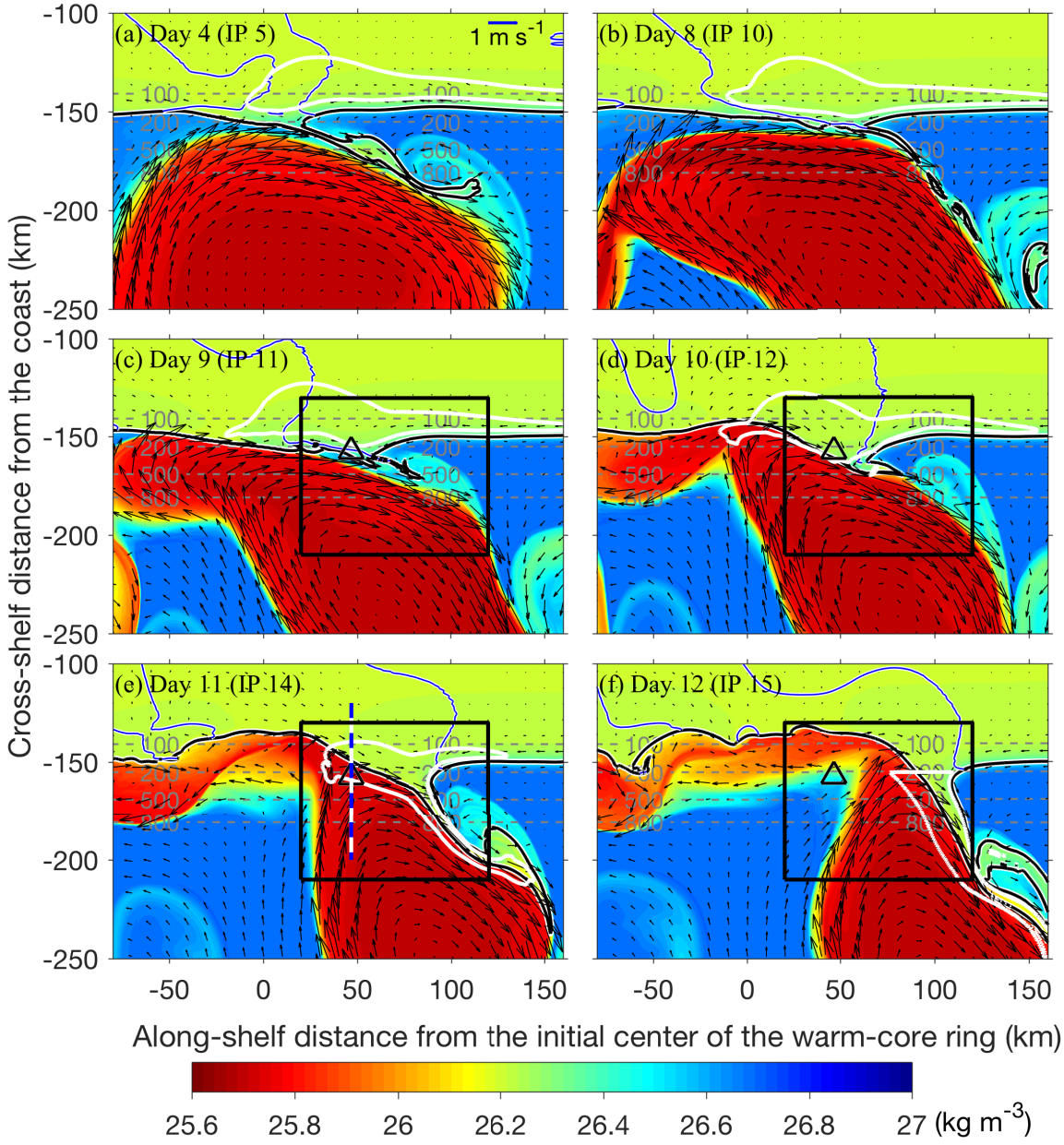

Fig. 8. Snapshots of the model surface density (color) and velocity (vectors) at different times. The black lines are the contour of 50% shelf water concentration; The thin blue lines are the contours of zero vertically-averaged along-shelf current on the shelf, outlining the shelf region under barotropic influence of the ring; The thick white lines depict the source region of the Day-12 streamer shelf water at different times obtained from the adjoint simulation; The triangles in (c-f) indicate the location of the model time series shown in Fig. 9 left column; The blue-white dashed line in (e) indicates the cross-shelf transect shown in Fig. 9 right column; The boxes in (d-f) depicts the area of view in Fig. 10; the grey dashed lines are isobath contours; 'IP' in each panel represents inertial period.

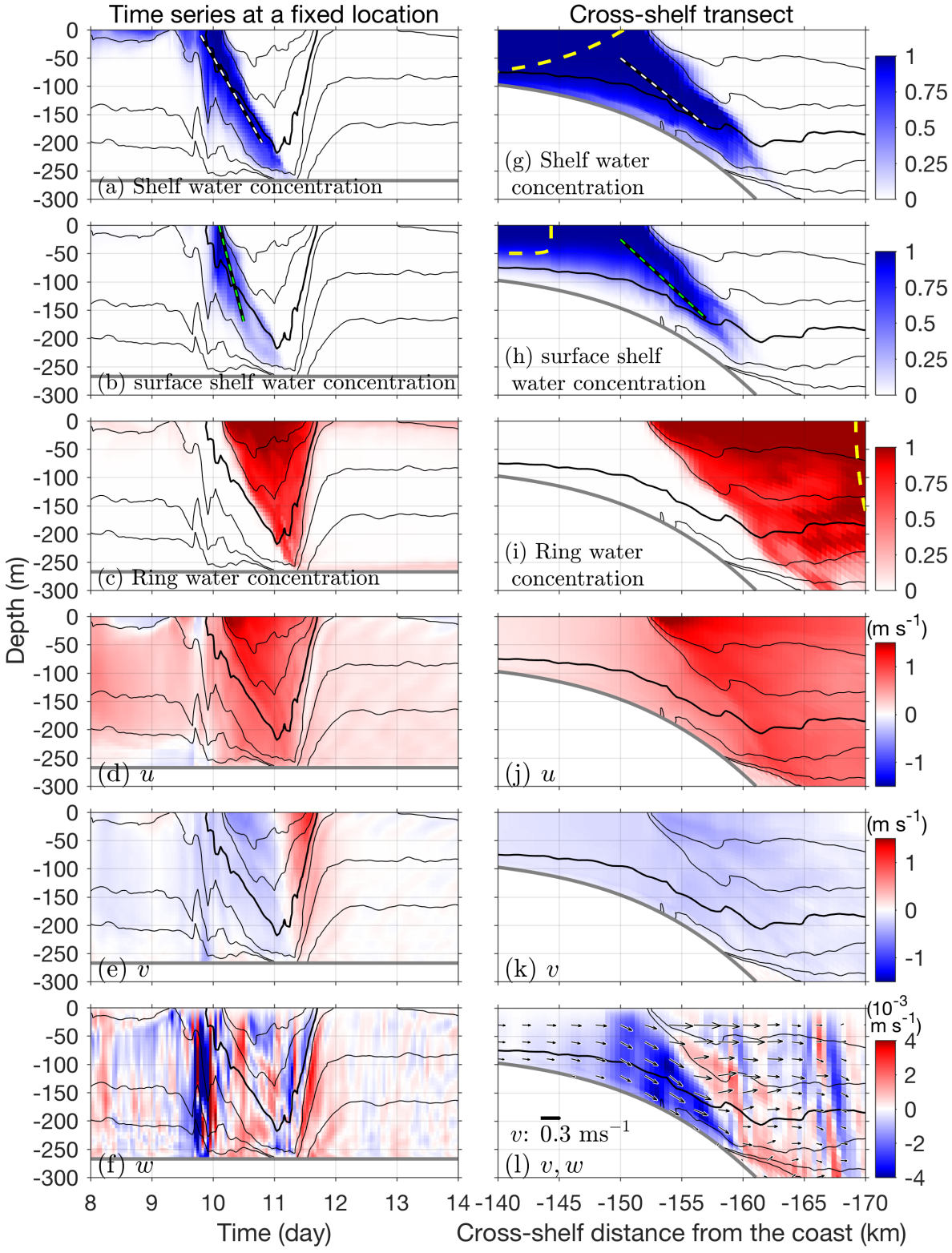

Fig. 9. (left) Time series of modeled (a) shelf water concentration (C_s), (b) surface shelf water concentration (C_{s2}), (c) ring water concentration (C_r), (d) eastward velocity, (e)

1141 northward velocity, and (f) vertical velocity at a fixed location (triangles in Fig. 8c-f)
1142 over the period of frontal subduction; (right) a cross-frontal transect of the same variables
1143 at x = 47 km and t = 11 days (blue dashed line in Fig. 8e). The black curves in all panels
1144 are contours of σ_θ with the interval of 0.2 kg m^{-3} and the 26.3 kg m^{-3} contour highlighted
1145 in bold. The dashed white lines in (a) and (g) highlight the subduction signals of the shelf
1146 water; the dashed green lines in (b) and (h) highlight the subduction signals of the surface
1147 shelf water; dashed yellow lines in (g), (h) and (i) represent the edges of the shelf,
1148 surface-shelf and ring waters, respectively, in the initial conditions.
1149

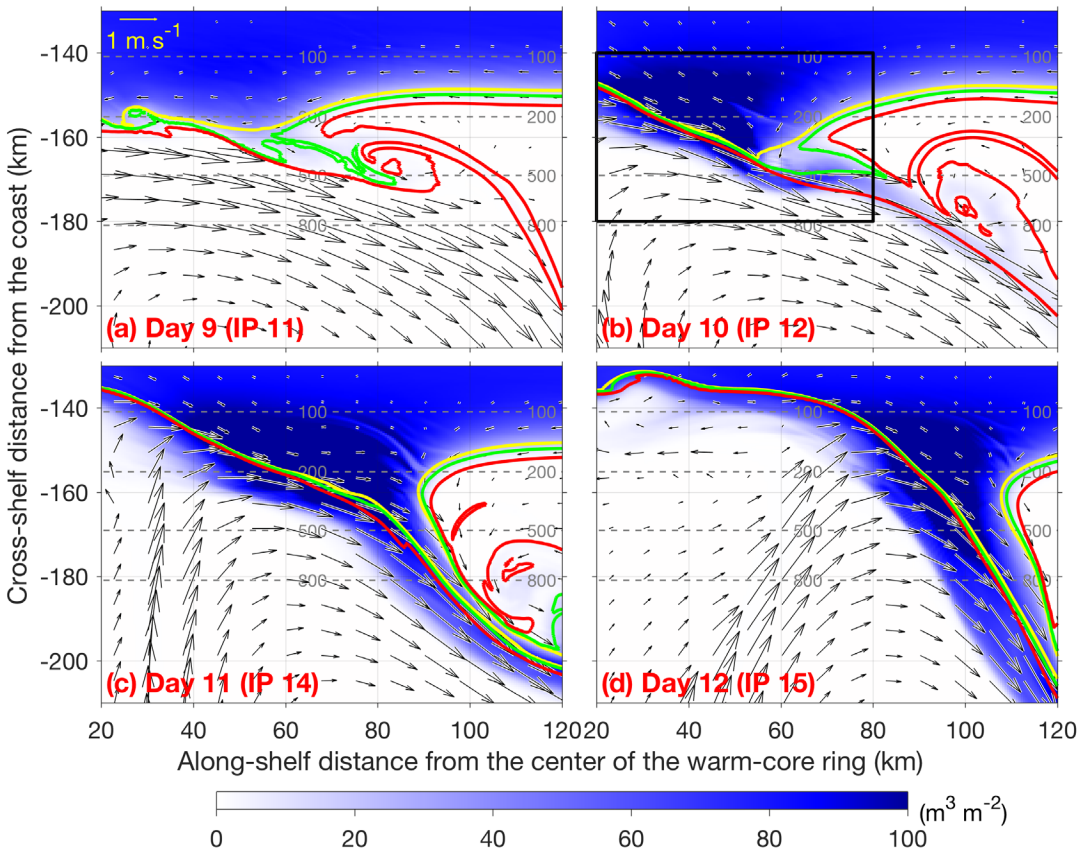

Fig. 10. Snapshots of vertically integrated shelf water concentration (i.e., the effective thickness of the shelf water; color) and contours of shelf water concentration C_s = 0.1 (red lines), 0.5 (green lines) and 0.75 (yellow lines) on sea surface. The vectors indicate the surface velocity with the scale at the top-left corner of (a), and the grey dashed lines are isobath contours. The box in (b) indicate the area of view in Fig. 11.

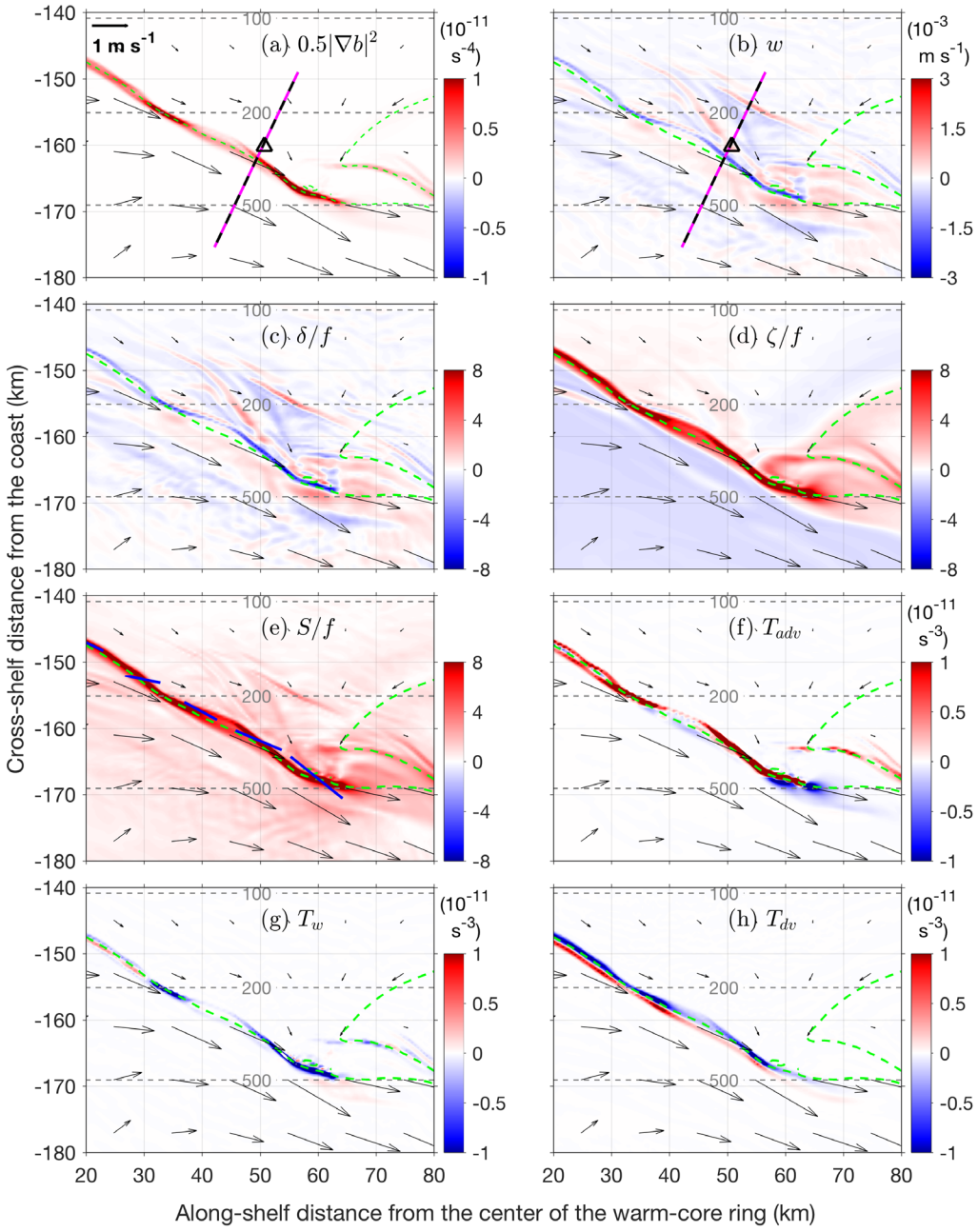

Fig. 11. Horizontal distribution of (a) frontal sharpness, (b) vertical velocity, (c) divergence, (d) relative vorticity, (e) stretch-strain rate (color) and principal deformation axis (thick blue lines), as well as the frontogenesis tendency terms due to (f) horizontal advection, (g) vertical advection, and (h) vertical mixing at $z = -3$ m and $t = 10$ days in a frontal region (black box in Fig. 10b). The dashed green lines are the contour of C_s (x, y, 0) = 0.5, indicating the location of the ring-edge front; The arrows are vectors of the surface velocity; The triangles in (a) and (b) indicate the location of the model time series in Fig. 9 left column; The dashed black-magenta lines in (a) and (b) indicate the location of the cross-frontal section in Fig. 12; The grey dashed lines are isobath contours.

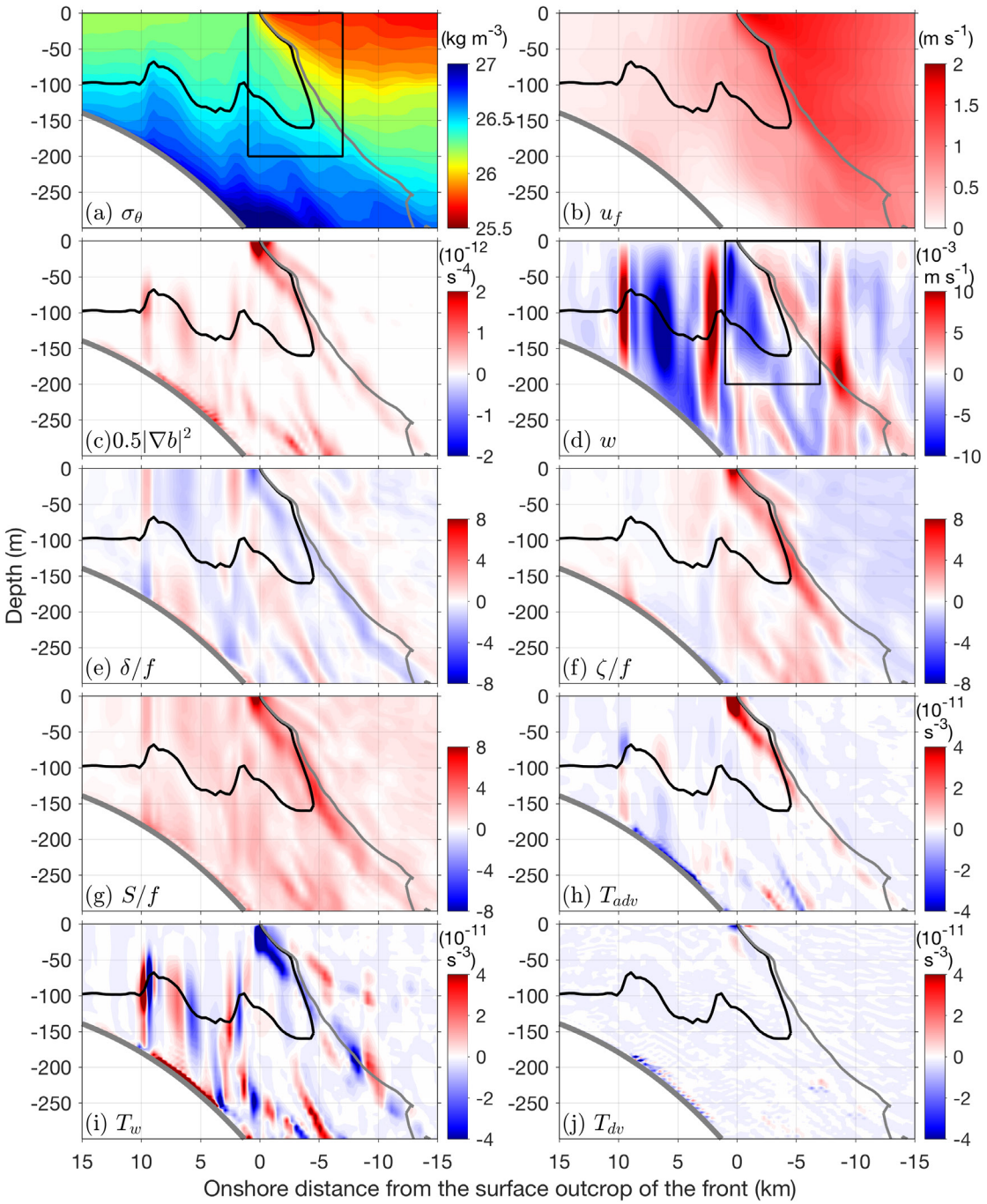

Fig. 12. Cross-frontal section of (a) σ_θ, (b) eastward velocity, (c) frontal sharpness, (d) vertical velocity, (e) divergence, (f) relative vorticity, (g) stretch-strain rate, as well as the frontogenesis tendency terms due to (h) horizontal advection, (i) vertical advection, and (j) vertical mixing along a line normal to the front (magenta lines in Fig. 11a-b) at t = 10 days. The black lines are the contours of C_s = 0.5, and the grey lines are the contours of C_r = 0.5. The boxes in (a) and (d) indicate the zoom-in region shown in Fig. 13.

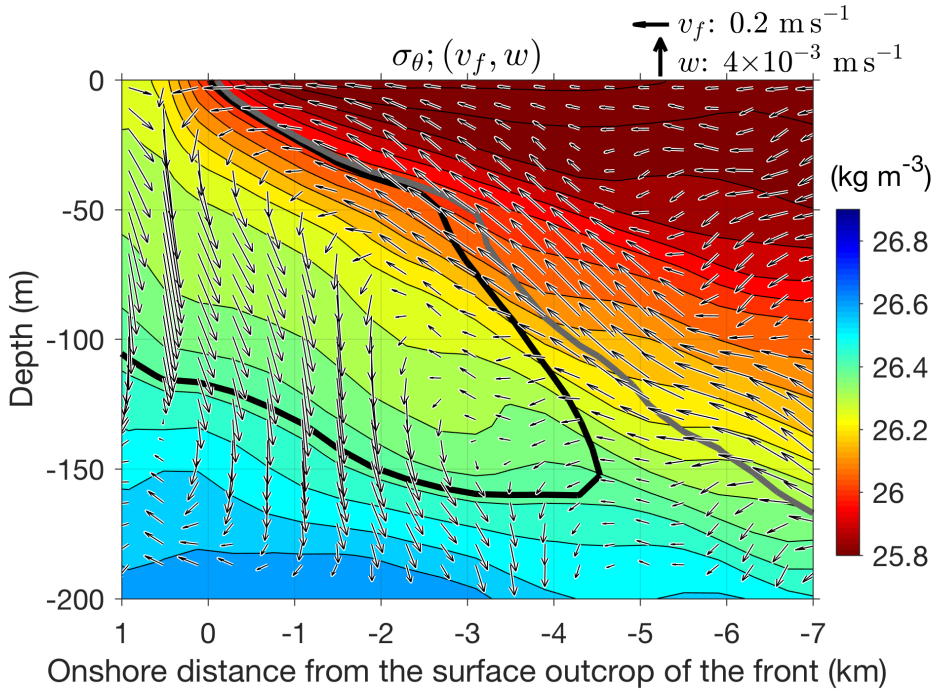

Fig. 13. A zoom-in view of the density (color) and secondary circulation (v_f and w; vectors) on the cross-frontal section (see the boxes in Figs. 12a and 12d for the area of view). Here, v_f is horizontal velocity in the cross-frontal direction. The scales of v_f and w are shown on the top-right corner. The black and grey lines is the contours of the shelf and ring water concentration of 0.5, respectively.

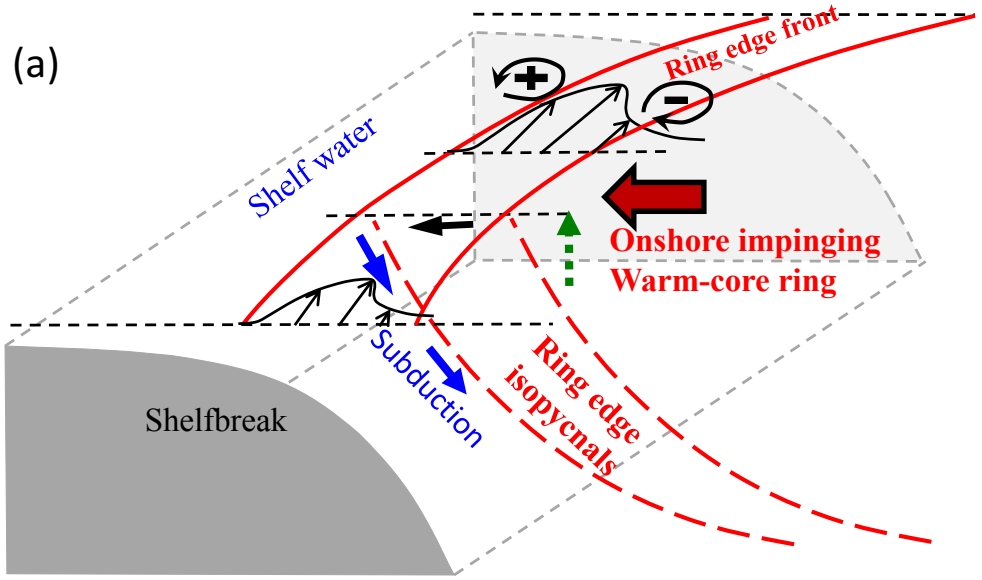

Fig. 14. A schematic of the 3D frontal subduction processes at the northern edge of the impinging warm-core ring. The big red arrow indicates the onshore migration of the WCR; the solid red lines represent two ring-edge isopycnals on the surface; the dashed red lines represent two ring-edge isopycnals on the vertical cross-shelf section; the thin black arrows represent the frontal jet on the surface. The blue, thick black and dashed green arrows depicts the secondary flow on a cross-frontal vertical section: the solid blue arrow indicates the subduction flow on the heavy side of the front; the thick black arrow indicates the cross-frontal onshore flow on the surface; the dashed green arrow indicates the upward flow on the light side of the front.

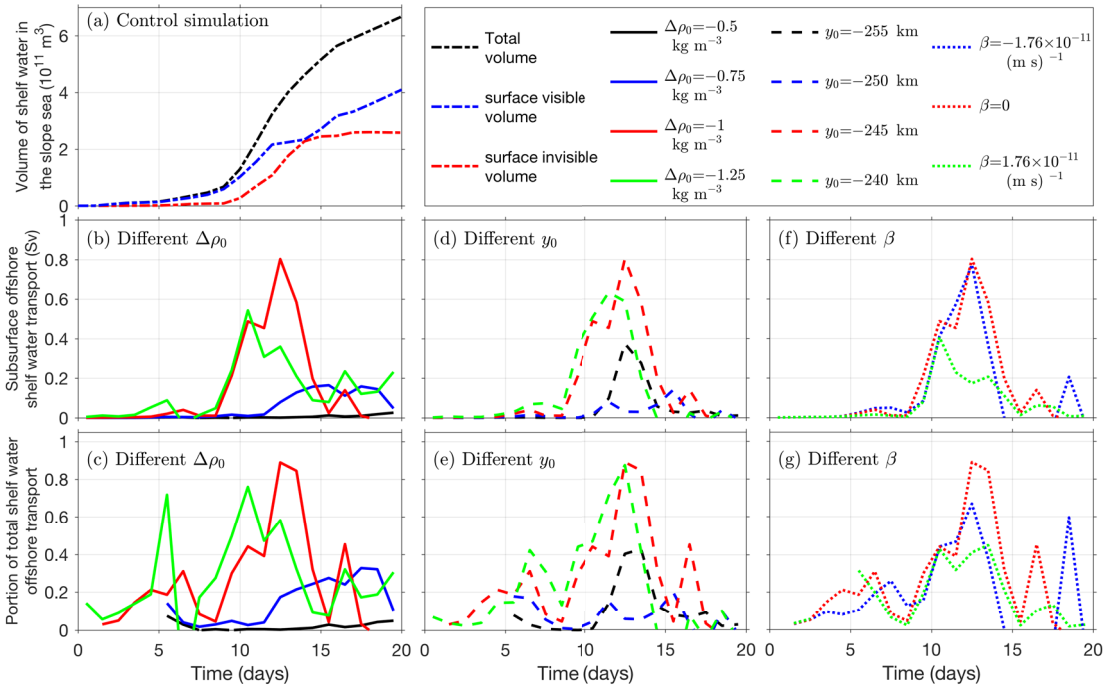

Fig. 15. Time series of modeled (a) volume of shelf water in the slope sea (offshore of the 200-m isobath), (b, d and f) surface-invisible offshore transport of the shelf water, and (c, e and g) fraction of the total offshore shelf water transport being surface invisible. The results in (a) are obtained from the control simulation; those in (b-c) are from sensitivity simulations of different ring water density anomaly ($\Delta\rho_0$); those in (d-e) are from sensitivity simulations of different initial cross-shelf position of the ring (y_0); and those in (f-g) are from sensitivity simulations of different β. The red curves in (b-g) are obtained from the control simulation. In (c), (e) and (g) only the faction at times of the total offshore shelf water transport exceeding 0.02 Sv is shown.